



# Eddy energy sources and mesoscale eddies in the Sea of Okhotsk

Dmitry V. Stepanov<sup>1</sup> · Nikolay A. Diansky<sup>2,3,4</sup> · Vladimir V. Fomin<sup>3</sup>

Received: 26 March 2018 / Accepted: 11 May 2018 / Published online: 29 May 2018  
© Springer-Verlag GmbH Germany, part of Springer Nature 2018

## Abstract

Based on eddy-permitting ocean circulation model outputs, the mesoscale variability is studied in the Sea of Okhotsk. We confirmed that the simulated circulation reproduces the main features of the general circulation in the Sea of Okhotsk. In particular, it reproduced a complex structure of the East-Sakhalin current and the pronounced seasonal variability of this current. We established that the maximum of mean kinetic energy was associated with the East-Sakhalin Current. In order to uncover causes and mechanisms of the mesoscale variability, we studied the budget of eddy kinetic energy (EKE) in the Sea of Okhotsk. Spatial distribution of the EKE showed that intensive mesoscale variability occurs along the western boundary of the Sea of Okhotsk, where the East-Sakhalin Current extends. We revealed a pronounced seasonal variability of EKE with its maximum intensity in winter and its minimum intensity in summer. Analysis of EKE sources and rates of energy conversion revealed a leading role of time-varying (turbulent) wind stress in the generation of mesoscale variability along the western boundary of the Sea of Okhotsk in winter and spring. We established that a contribution of baroclinic instability predominates over that of barotropic instability in the generation of mesoscale variability along the western boundary of the Sea of Okhotsk. To demonstrate the mechanism of baroclinic instability, the simulated circulation was considered along the western boundary of the Sea of Okhotsk from January to April 2005. In April, the mesoscale anticyclonic eddies are observed along the western boundary of the Sea of Okhotsk. The role of the sea ice cover in the intensification of the mesoscale variability in the Sea of Okhotsk was discussed.

**Keywords** Mesoscale variability · Sea of Okhotsk · Eddy kinetic energy · Baroclinic instability · Barotropic instability

## 1 Introduction

Studying mesoscale variability is critical for improving our understanding about how the basin circulation functions (Lapeyre 2009; Stammer 1997; Koshlyakov and Monin 1978). Analyzing this variability, it is necessary in its quantitative description. In order to uncover causes and mechanisms of the generation of the mesoscale variability, it is necessary to understand the role of the basin-scale

circulation and atmospheric forcing in this generation. Instability (in particular, baroclinic and barotropic) of the basin-scale currents is underlying an interaction between the basin-scale circulation and mesoscale motions (Stammer 1997; Ferrari and Wunsch 2010). A quantitative estimation of this interaction is necessary to estimate a contribution of this instability in the generation of the mesoscale variability (von Storch et al. 2012; Stammer 1997). Also, it is very important to estimate a contribution of the atmospheric forces including wind power input in the generation of the mesoscale dynamics (Wunsch 1998). Challenges of studying mesoscale variability at high latitudes are associated with decreasing spatial scale of the mesoscale motions and the existence of the vast scape of the basin covered by sea ice.

The Sea of Okhotsk is one of the marginal seas of the northwestern Pacific Ocean. This sea is situated at high latitudes and, being in the southernmost sea, is covered by sea ice during the year. The Okhotsk Sea circulation is a subject of high scientific interest (Ohshima et al. 2002; Mizuta et al. 2003), because this basin is the source of

---

Responsible Editor: Eric Deleersnijder

✉ Dmitry V. Stepanov  
stepnovster@gmail.com

- <sup>1</sup> V.I. Il'ichev Pacific Oceanological Institute, Vladivostok, Russia
- <sup>2</sup> Lomonosov Moscow State University, Moscow, Russia
- <sup>3</sup> N.N. Zubov State Oceanographic Institute, Moscow, Russia
- <sup>4</sup> Institute of Numerical Mathematics of the RAS, Moscow, Russia

intermediate water in the western North Pacific (Talley 1991; Gladyshev et al. 2003; Fukamachi et al. 2004). In winter, dense shelf waters generated over the northwestern shelf of the Sea of Okhotsk are transported by the East-Sakhalin Current (ESC) in the Kuril Basin, where they are mixed by mesoscale eddies and tides. Shcherbina et al. (2004), based on the datasets obtained from the moorings deployed at the northwestern Sea of Okhotsk, have discovered sharp changes in the density increase in late February. Authors supposed that these sharp density changes were induced by baroclinic instability of the density front. The basin-scale circulation in the Sea of Okhotsk is cyclonic and the ESC is a major component of this circulation (Luchin 1998; Ohshima et al. 2002). The ESC is a southward current and follows along the western boundary of this sea. Ohshima et al. (2002), using satellite-tracked drifter data, showed that the ESC consists of the nearshore and offshore components. The nearshore component spreads over the eastern Sakhalin shelf and the offshore component flows over the continental slope and, being the part of the basin-scale cyclonic gyre, covers the central part of the Sea of Okhotsk. Smizu and Ohshima (2006) have established that wind stress is a major driver of the basin-scale circulation in the Sea of Okhotsk. The dominating positive wind stress curl drives a cyclonic gyre in the central part of the Sea of Okhotsk and the offshore component of the ESC. The alongshore wind stress component is a major driver of the barotropic component of the alongshore component of the ESC. The baroclinic part of the alongshore component of the ESC is associated with the Amur River discharge (Mizuta et al. 2003). The strong seasonal variability of the wind stress promotes the strong seasonal variability of the circulation in the Sea of Okhotsk. In addition, heat and freshwater fluxes over the Sea of Okhotsk exhibit seasonal variability and their impact on the basin-scale circulation is corrected by sea ice cover.

By studying the energy of the ocean circulation, Ferrari and Wunsch (2010) have found that the considerable portion of this energy is associated with the mesoscale eddies in comparison with the large-scale circulation energy. In addition, the mesoscale eddies are responsible for the transport of heat and salt (Chelton et al. 2011). The spatial scale of the mesoscale eddies is associated with the first baroclinic Rossby radius of deformation ( $\lambda_1$ ) (Chelton et al. 1998), which changes from 100–200 km at low latitudes to about 10 km at high latitudes. The causes and mechanisms of the mesoscale eddy generation were subject of numerous studies (Zhan et al. 2016; Yang et al. 2013; von Storch et al. 2012). However, because of challenges associated with studies of the mesoscale eddies at high latitudes and marginal seas, this problem is far from complete. By

investigating mesoscale variability both the World Ocean and marginal seas, one of the approaches is based on an analysis of the EKE budget. von Storch et al. (2012) have presented a methodology and carried out the comprehensive analysis of sources and sinks of the EKE in the World Ocean based on numerical simulations. Authors have estimated contributions of baroclinic and barotropic instabilities of the large-scale currents to the generation of the mesoscale variability. It was confirmed that the baroclinic instability of the large-scale circulation is a dominating mechanism of the mesoscale eddy generation (Stammer 1997). Mesoscale eddies in the Sea of Okhotsk are the subject of high scientific interest. Ohshima et al. (2002), based on satellite-tracked drifter observations, showed that anticyclonic eddies with the diameter varying from 100 to 200 km dominate over the Kuril Basin and eddy kinetic energy (EKE) exceeds mean kinetic energy (MKE) from 3 to 20 times. Ohshima et al. (2005) have established that a major mechanism of the eddy generation over the Kuril Basin is the baroclinic instability of the tidal front induced by intense tidal mixing near the Kuril Straits. Ohshima and Wakatsuchi (1990) have investigated the mesoscale variability over the southwestern Kuril Basin near the Soya Strait and establish that the generation mechanism of this variability is the barotropic instability of the Soya Current. Uchimoto et al. (2007) have studied the impact of the Soya Current transport on the mesoscale variability. Thermal infrared images with very high spatial resolution have revealed features of the sub-mesoscale variability (the eddy diameter ranging from 2 to 30 km) near the Kuril Islands (Nakamura et al. 2012). In the abovementioned studies, the mesoscale variability in the Sea of Okhotsk was studied mainly during the ice-free period. Thus, the whole picture of the mesoscale variability of this sea is not fully uncovered.

In this study, based on numerical simulation outputs on an eddy-permitting resolution, the mesoscale variability is analyzed in the Sea of Okhotsk. Wind power input and baroclinic and barotropic instabilities of the ESC are considered as main sources of the EKE. The paper is organized as follows. Section “2” describes the model configuration. Validation of the model is presented in Section “3.” Spatial distribution of the EKE in the Sea of Okhotsk is presented in Section “4.” Rates of energy conversion and main sources of the EKE in the Sea of Okhotsk as well as a typical picture of the mesoscale variability on the eastern shelf of Sakhalin Island are presented in Section “5.” Discussion of the impact of the sea ice cover on the EKE budget and the contribution of different factors in the EKE balance are presented in Section “5.” Summary of the main results is presented in Section “6.”

## 2 Model description

The numerical simulations are carried out with a numerical ocean model developed in the Institute of Numerical Mathematics of the Russian Academy of Sciences (the Institute of Numerical Mathematics Ocean Model or INMOM). The INMOM is a sigma-coordinate ( $\sigma$ ) model based on primitive equations of the ocean dynamics with hydrostatic and Boussinesq approximations (Marchuk et al. 2005; Gusev and Diansky 2014; Diansky et al. 2016; Zalesny et al. 2017). Using the relations  $Z = \sigma h + \zeta$  and  $h = H - \zeta = Z_\sigma$  and assuming that  $\zeta \ll H$ , we present briefly the basic model equations in the generalized coordinates ( $p, q$ ) as the following:

$$D_t U - (f + \gamma) V H = -\frac{Z_\sigma}{r_p} \left( \frac{1}{\rho_0} P_p + \frac{1}{\rho_0} \frac{\partial P_a}{\partial p} - g \frac{\partial \zeta}{\partial p} \right) + \frac{\partial}{\partial \sigma} \frac{\nu}{Z_\sigma} \frac{\partial U}{\partial \sigma} + F U, \tag{1}$$

$$D_t V + (f + \gamma) U H = -\frac{Z_\sigma}{r_q} \left( \frac{1}{\rho_0} P_q + \frac{1}{\rho_0} \frac{\partial P_a}{\partial q} - g \frac{\partial \zeta}{\partial q} \right) + \frac{\partial}{\partial \sigma} \frac{\nu}{Z_\sigma} \frac{\partial V}{\partial \sigma} + F V, \tag{2}$$

$$\frac{1}{r_q r_p} \left( \frac{\partial U Z_\sigma r_q}{\partial p} + \frac{\partial V Z_\sigma r_p}{\partial q} \right) + \frac{\partial \omega}{\partial \sigma} = \frac{\partial \zeta}{\partial t}, \tag{3}$$

where  $r_q$  and  $r_p$  are metric coefficients,  $\gamma = \frac{1}{r_q r_p} \left( V \frac{\partial r_q}{\partial p} - U \frac{\partial r_p}{\partial q} \right)$ ,  $g$  is the gravitational acceleration,  $\mathbf{U}(U, V, \omega)$  is the velocity vector,  $f$  is the Coriolis parameter,  $P_a$  is the atmospheric pressure,  $\zeta$  is the sea level deviation from its unperturbed state,  $H$  is the depth, and  $\nu$  is the vertical viscosity. The transport operator ( $D_t$ ) is the semi-divergent symmetrized form (Zalesny et al. 2017) and the horizontal viscosity operator ( $F$ ) is the divergent form and includes the second- and fourth-order operators (Zalesny et al. 2017). To avoid drawback of sigma coordinate models, horizontal pressure gradient components are calculated as the following (Marchuk et al. 2005):

$$P_p = \frac{1}{2} g \left( \frac{\partial}{\partial p} \left( Z_\sigma \int_0^\sigma (\rho - \sigma \frac{\partial \rho}{\partial \sigma}) d\sigma \right) - \sigma \left( \frac{\partial Z_\sigma}{\partial p} \rho - Z_\sigma \frac{\partial \rho}{\partial p} \right) \right), \tag{4}$$

$$P_q = \frac{1}{2} g \left( \frac{\partial}{\partial q} \left( Z_\sigma \int_0^\sigma (\rho - \sigma \frac{\partial \rho}{\partial \sigma}) d\sigma \right) - \sigma \left( \frac{\partial Z_\sigma}{\partial q} \rho - Z_\sigma \frac{\partial \rho}{\partial q} \right) \right). \tag{5}$$

Equations 1–3 are complemented by the following equations:

$$D_t \theta = \frac{\partial}{\partial \sigma} \frac{\nu_\theta}{H} \frac{\partial \theta}{\partial \sigma} + D_\theta \theta + \frac{\partial R}{\partial \sigma}, \tag{6}$$

$$D_t S = \frac{\partial}{\partial \sigma} \frac{\nu_S}{H} \frac{\partial S}{\partial \sigma} + D_S S, \tag{7}$$

$$\rho = \hat{\rho}(\theta, S + 35\text{‰}, p_w) - \hat{\rho}(0, 0, \rho_0 g \sigma H), \tag{8}$$

where  $\theta$  is the potential temperature;  $S$  is the salinity deviation from 35‰;  $p_w$  is the water pressure;  $\rho_0$  is the reference density amounting to 1025 kg m<sup>-3</sup>;  $R$  is the penetrative solar radiation flux; and  $\nu_\theta$  and  $\nu_S$  are the vertical diffusivity of  $\theta$  and  $S$ , respectively;  $D_S$  and  $D_\theta$  are the horizontal operators of lateral diffusion of  $\theta$  and  $S$ , respectively. Note that  $D_S$  and  $D_\theta$  are the divergent forms. Equation of the water state  $\hat{\rho}(\theta, S + 35\text{‰}, p_w)$  is a nonlinear equation (Brydon et al. 1999), which enables reducing the drawback of sigma coordinate models (Marchuk et al. 2005). INMOM incorporates a sea ice model, which accounts for the sea ice dynamics and its thermodynamics including the generation and melting of sea ice and transformation of snow to sea ice (Yakovlev 2003). The algorithm of the numerical solution for the INMOM is based on the method of multi-component splitting (Marchuk et al. 2005).

To simulate the circulation in the Sea of Okhotsk, we use the INMOM model with the horizontal resolution of about 3.5 km and 35 sigma-level thickening near the sea surface to resolve density stratification. The Sea of Okhotsk connects with the northwestern Pacific Ocean by means of the Kuril Straits, with the Japan/East Sea by means of the Soya and Tatar Straits. So, to avoid setting up the open boundary conditions in the Sea of Okhotsk Straits, the model domain spans the Sea of Okhotsk, Japan/East Sea, and the northwestern Pacific Ocean. To obtain quasi-uniform spatial resolution, we use a spherical coordinate system with a pole, situated at the point with the coordinates of 25.5° E, 22.4° N. Thus, an equator of this coordinate system crosses the Sea of Okhotsk and the Japan/East Sea. Figure 1 shows the bottom topography of the model domain, which was extracted from the GEBCO dataset (Becker et al. 2009). To avoid the drawback of sigma models, we apply the nine-point smoothing of the model bottom topography 10 times. According to the bottom topography, the Sea of Okhotsk features the wide northern shelf, the deep Central Basin, and the deepest Kuril Basin situated in the southeastern part of this sea. Because the  $\lambda_1$  is a spatial scale of mesoscale motions (Pedlosky 1987; Chelton et al. 1998; Stammer 1997), in order to resolve these motions, a model spatial resolution has to resolve the  $\lambda_1$ . Stepanov

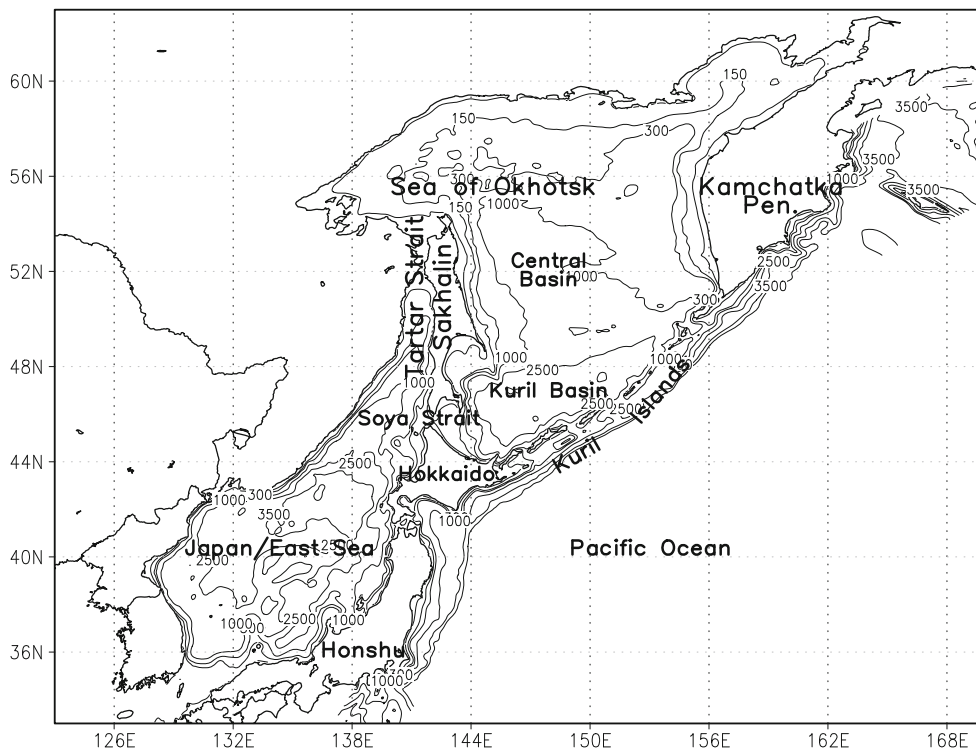


**Fig. 1** Bottom topography (m) of the model domain in the geographic coordinate system

(2017) showed that  $\lambda_1$  varies from 1.5 to 2 km over the northern shelf of the Sea of Okhotsk, from 8 to 10 km in the Central Basin, and from 18 to 20 km over the Kuril Basin. Thus, the used model resolution enables taking into account mesoscale variability in the Sea of Okhotsk, at least, southward of  $52^\circ$  N. To avoid artificial reduction of the available potential energy associated with the deflection of isopycnal surfaces from the state of rest; for potential temperature and salinity, we use the geopotential Laplacian framework with the coefficient of  $10 \text{ m}^2 \text{ s}^{-1}$  for both variables. Vertical turbulent processes are parameterized according to the Pacanowski-Philander parameterization (Pacanowski and Philander 1981), where  $\nu$  varies from  $10^{-4}$  to  $2.5 \times 10^{-2} \text{ m}^2 \text{ s}^{-1}$  and  $\nu_\theta$  equals  $\nu_S$  and varies from  $10^{-5}$  to  $5 \times 10^{-3} \text{ m}^2 \text{ s}^{-1}$ . Convective mixing is parameterized by maximum viscosity and diffusivity, which amount to  $2.5 \times 10^{-2}$  and  $5 \times 10^{-3} \text{ m}^2 \text{ s}^{-1}$ , respectively.

Sensible and latent heat fluxes, short- and long-wave radiations, momentum flux, and net salt flux, containing precipitation, evaporation, and climatological runoff contributions, are derived with the bulk-formulae (Stepanov et al. 2014; Diansky et al. 2016; Large and Yeager 2009). Atmospheric parameters for atmospheric forcing were extracted from the ERA-Interim dataset (Dee et al. 2011) with the spatial resolution of  $0.75^\circ \times 0.75^\circ$  from 1979 to 2009. Wind speed at the height of 10 m and air temperature and absolute humidity at the height of 2 m have the time resolution of 6 h.

In this study, we used a model configuration (hereafter, *Control* experiment) taking into account only thermodynamics of the sea ice and the wind stress ( $\tau_{wind}$ ) is assessed under an open water approximation

$$\tau_{wind} = \rho_a C_D |\mathbf{u}_{wind} - \mathbf{u}_s| (\mathbf{u}_{wind} - \mathbf{u}_s), \quad (9)$$

where  $\mathbf{u}_{wind}$  and  $\mathbf{u}_s$  are the wind speed and sea surface velocity, respectively,  $\rho_a$  is the air density amounting to  $1.3 \text{ kg m}^{-3}$ . The coefficient  $C_D$  is set as following  $C_D = (1.1 + 0.0004 \cdot |\mathbf{u}_{wind} - \mathbf{u}_s|) \cdot 10^{-3}$ . At assessing the stress on the sea surface as according to relation Eq. 9, we neglect the stress between the sea ice and water. However, we will show that taking into account the sea ice cover at the estimation of wind stress does not result in significant qualitative and quantitative changes of the circulation in the Sea of Okhotsk. Under the long-term numerical simulations, the simulated potential temperature and salinity can deviate from their climatological values. In order to avoid these deviations, the simulated potential temperature and salinity averaged in the upper 20 m are nudged to their climatological monthly mean values with the relaxation parameter amounting to  $10^{-5} \text{ m s}^{-1}$  for both variables. On solid boundaries, the no-normal flow and free-slip boundary conditions are applied and heat and salt fluxes are equal to 0. Near each open boundary, we reserve a region with width of about  $1^\circ$  from the sea surface to the bottom, where the potential temperature and

salinity, derived from the advection-diffusion equation, are nudged to their climatological monthly mean values with the relaxation parameter of 3 h. Note that we neglect the tidal impact on the circulation in the Sea of Okhotsk. No-normal flow and free-slip boundary conditions are applied on the open boundaries.

Initial potential temperature and salinity are extracted from the datasets (Locarnini et al. 2013; Zweng et al. 2013). Preliminarily, we simulated a circulation during four years under yearly repeating atmospheric forcing corresponding to 1979. Initial conditions for potential temperature and salinity corresponded to June 1979. During four years the circulation in the Sea of Okhotsk and the Japan/East Sea attains a quasi-steady state. Numerical simulation outputs, obtained at the end of fourth year, were used as initial conditions for numerical simulations with the atmospheric forcing varying from 1979 to 2009. In this study, we analyze numerical simulation outputs from 2005 to 2009.

### 3 Model validation. General circulation and its variability

Let us consider a spatial structure of the long-term mean circulation in the Sea of Okhotsk obtained from the

numerical simulations from 2005 to 2009. Figure 2 shows the long-term seasonal mean velocity field and the mean kinetic energy (MKE) at the sub-surface depth and their changes during the year. The MKE per unit mass is

$$MKE = \frac{1}{2} (\bar{u}^2 + \bar{v}^2), \tag{10}$$

where  $u$  and  $v$  are zonal and meridional velocity components, respectively. The overbar denotes the long-term monthly mean average (from 2005 to 2009). According to the numerical simulations, the basin-scale circulation consists of a northward current called the West Kamchatka Current (Matsuda et al. 2015), which follows along the western coast of the Kamchatka peninsula, a boundary current over the northern shelf of the Sea of Okhotsk and a southward current following along the western boundary of this sea, which is known as the ESC. This current consists of alongshore and offshore components. The alongshore component originates in the northwestern part of the Sea of Okhotsk and follows along the eastern coast of Sakhalin Island up to the northeastern coast of Hokkaido Island (see, Fig. 1). The offshore component is a component of the cyclonic gyre spanning the Central Basin of the Sea of Okhotsk. This component of the ESC follows over the continental slope and turn to east at 47°–48° N. These features

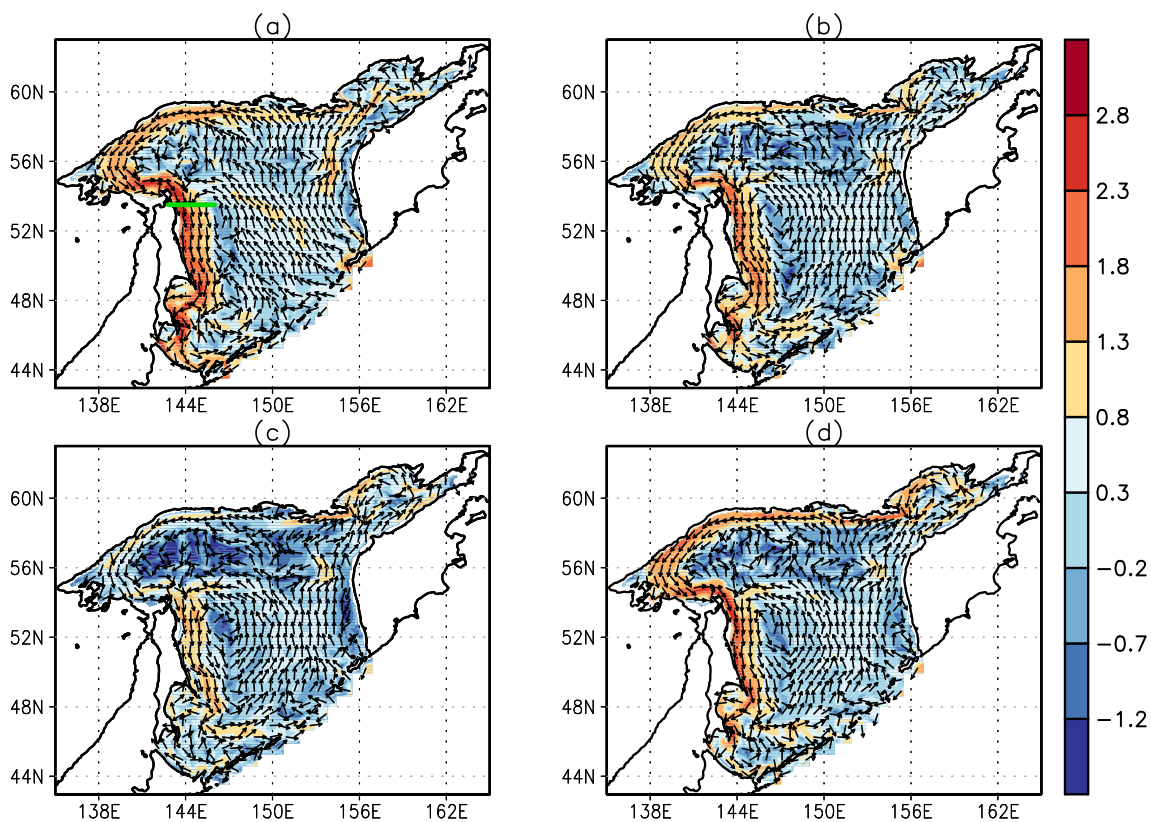


**Fig. 2** Long-term seasonal mean velocity field (vector, direction) and MKE ( $\log_{10} \text{ cm}^2 \text{ s}^{-2}$ ) at 30 m depth in **a** winter, **b** spring, **c** summer, and **d** autumn. Green line denotes a zonal transect at 53.5° N from 142.8° E to 146° E

of the basin-scale circulation in the Sea of Okhotsk are consistent with those derived from drifter and altimetry data (Ohshima et al. 2002; Mizuta et al. 2003) as well as features obtained from numerical simulations both on the coarse resolution (Smizu and Ohshima 2006) and the finer resolution (Matsuda et al. 2015). It should be noted that according to the study (Ohshima et al. 2002), the turning of the offshore component took place at  $48^{\circ}$ – $51^{\circ}$  N. However, the turning of the offshore component obtained from our numerical simulations takes place southward of  $48^{\circ}$  N. We suppose that this discrepancy results from the underestimation of the intensity of the offshore component due to insufficiently intensive wind stress derived from the ERA–Interim dataset. The distribution of MKE indicates that the intensity of the ESC predominates on the intensity of the other parts of the basin scale cyclonic circulation of the Sea of Okhotsk. The ESC shows a pronounced seasonal variability with its maximum intensity in winter and its minimum intensity is observed in summer. The pronounced seasonal variability of the ESC is consistent with the seasonal variability of the ESC derived from the natural measurements (Mizuta et al. 2003) and obtained from the numerical simulations (Smizu and Ohshima 2006).

We estimated the transport of the ESC at  $53.5^{\circ}$  N, which quantitatively characterizes the ESC intensity. Figure 3 shows the long-term monthly mean transport of the ESC (see, Fig. 3a) and its monthly mean values from 2005 to 2009 (see Fig. 3b). According to these estimations, the long-term annual ESC transport equals to about 3 Sv ( $1 \text{ Sv} = 10^6 \text{ m}^3 \text{ s}^{-1}$ ), which is less than the ESC transport derived from the drifter data (from 4 to 9 Sv) (Ohshima et al. 2002). The ESC transport shows a pronounced seasonal variability. Maximum of the ESC transport, amounting to 4.1 Sv, is observed in winter (in January) and its minimum amounting to 1.5–1.7 Sv is observed in summer

(in July). The pronounced seasonal variability of the ESC transport is consistent with that derived from current measurements (Mizuta et al. 2003) and obtained from numerical simulations both on the coarse (Smizu and Ohshima 2006) and finer resolutions (Matsuda et al. 2015). However, we observe an underestimation of the ESC transport in winter. On the other hand, in summer, the ESC transport differs weakly from that derived from current measurements (Mizuta et al. 2003). So, this underestimation could be a consequence of insufficiently intensive wind stress derived from the ERA–Interim dataset. Significant changes of the ESC transport are observed on interannual time scales. From 2005 to 2009, the maximum of the ESC transport varies from 6 to 4 Sv (see Fig. 3b).

Let us consider a vertical structure of the simulated velocity field on the eastern Sakhalin shelf and compare this structure with that derived from current measurements (Mizuta et al. 2003). Figure 4 shows the vertical structure of the meridional velocity derived from the numerical simulations when the ESC transport attains extremal values. According to this vertical structure, the alongshore component of the ESC features a typical velocity more  $0.3 \text{ m s}^{-1}$  near the sea surface in the northeastern part of Sakhalin Island. The offshore component of the ESC spreads over the continental slope, where the meridional velocity attains the values of  $0.1$ – $0.11 \text{ m s}^{-1}$  in the upper layer from the sea surface to the depths of 150–180 m. The vertical structure of the long-term mean meridional velocity points out the underestimation of the intensity of the offshore component of the ESC.

In the end of this section, we consider a potential density field obtained from the numerical simulations. Figure 5 shows a vertical structure of the long-term mean simulated potential density on the zonal transect at  $53^{\circ}$  N. We find that isopycnals rise from east to west and then drop

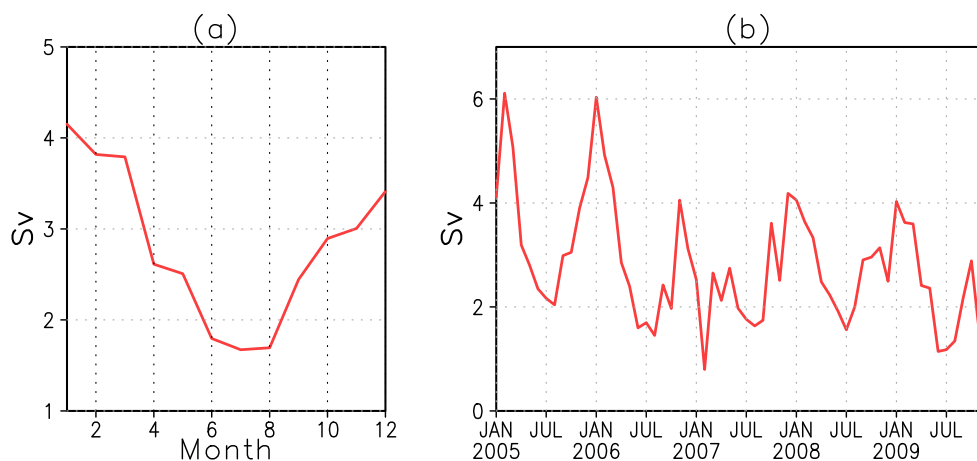


**Fig. 3** Transport of the East-Sakhalin Current (Sv) on the zonal transect (see Fig. 2) obtained from numerical simulation outputs: **a** its long-term monthly mean (from 2005 to 2009) and **b** its monthly mean variations

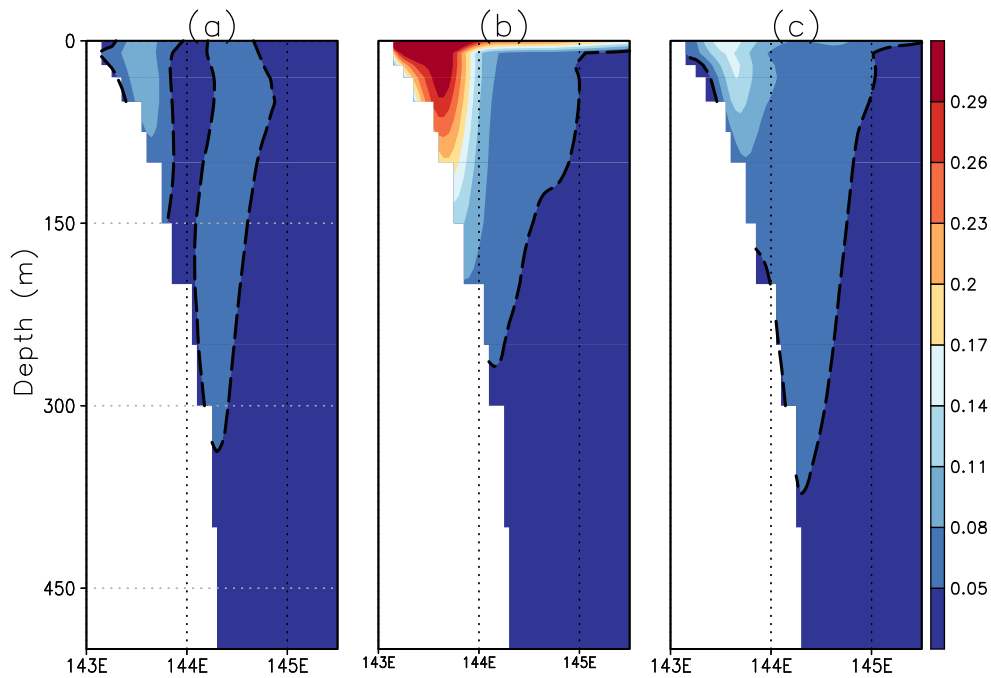


**Fig. 4** Vertical sections of the long-term monthly mean meridional velocity derived from the numerical simulations on the zonal transect (see Fig. 2) in **a** July, **b** January, and **c** March. Dashed line denotes the isoline of  $0.05 \text{ m s}^{-1}$ . Positive value indicates a southward meridional velocity

near the western boundary of the Sea of Okhotsk. This vertical structure of the simulated isopycnal surfaces is consistent with that derived from current measurements and from numerical simulations on the coarse resolution. The rising of the isopycnals from the east to west and then

their dropping over the continental slope point out that the offshore component of the ESC is an analog of the western boundary current in the cyclonic gyre spanning the Central Basin of the Sea of Okhotsk. Maximal rising of the isopycnal surfaces is observed on the depths from 300

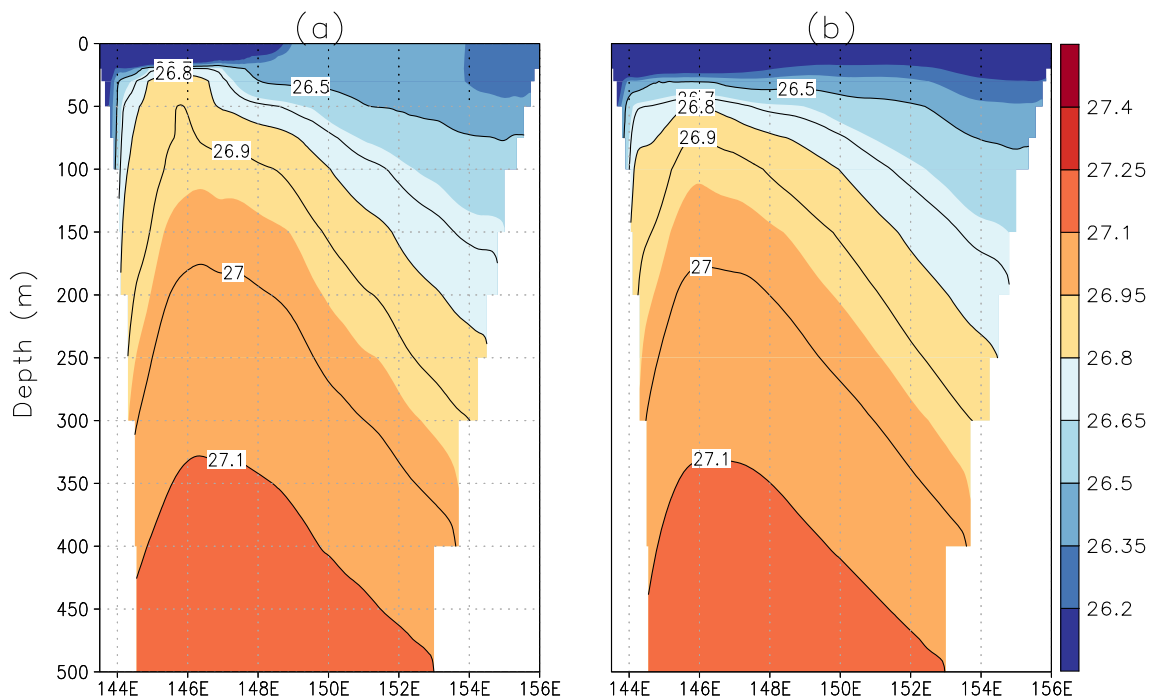


**Fig. 5** Vertical section of density ( $\sigma_\theta$ ,  $\text{kg m}^{-3}$ ) averaged from 2005 to 2009, on the zonal transect at  $53^\circ \text{ N}$ , **a** its distribution on February and **b** its long-term mean distribution

to 400 m. It is consistent with the observations (Mizuta et al. 2003) and the numerical simulations on the coarse resolution (Smizu and Ohshima 2006).

Thus, the validation of our numerical simulations showed that the used model configuration reproduces the basin-scale circulation in the Sea of Okhotsk with the underestimation of the offshore component of ESC. Therefore, the results of this study would be applicable, mainly, over the eastern Sakhalin shelf.

#### 4 Eddy kinetic energy in the Sea of Okhotsk

In this section, we analyze the EKE in the Sea of Okhotsk estimated from numerical simulation outputs. Because the intensity of the circulation in the Sea of Okhotsk shows the pronounced seasonal variability (see Section “3”), we apply the long-term monthly mean averaging and “eddies” are defined as perturbations from the mean flow (10). In order to estimate the EKE, we used the relation

$$\text{EKE} = \frac{1}{2} \rho_0 (\overline{u'^2} + \overline{v'^2}), \quad (11)$$

where  $\overline{u'^2}$  and  $\overline{v'^2}$  are the long-term monthly mean squares of the eddy components of velocities, respectively. The prime denotes a deflection from the mean value. These long-term monthly mean squares were estimated with the relation (von Storch et al. 2012)

$$\overline{a' \cdot b'} = \overline{a \cdot b} - \bar{a} \cdot \bar{b}, \quad (12)$$

where  $a$  and  $b$  are the analyzed variables (velocity components or the density deflection from the  $\rho_0$ ). In relation (12), the analyzed variables and two-variable products were accumulated at every 24 h. Note that the interannual signal of the basin-scale circulation is included in the EKE under such definition of eddies (11–12). However, compared to the dominant seasonal variability of the basin-scale circulation, its interannual variability is much weaker. In addition, we established that EKE, averaged over the whole of the Sea of Okhotsk, is two times higher than MKE during the year. Thus, the contribution of the mesoscale variability into the EKE dominates over that of the interannual variability of the basin-scale circulation and the latter could be neglected.

We consider four seasons: winter (December, January, and February), spring (March, April, and May), summer (June, July, and August), and autumn (September, October, and November). Figure 6 shows basin-averaged EKE and MKE profiles over the Sea of Okhotsk in winter and summer. In winter, maximal values of the EKE are observed near the sea surface and exceed up to two times maximal

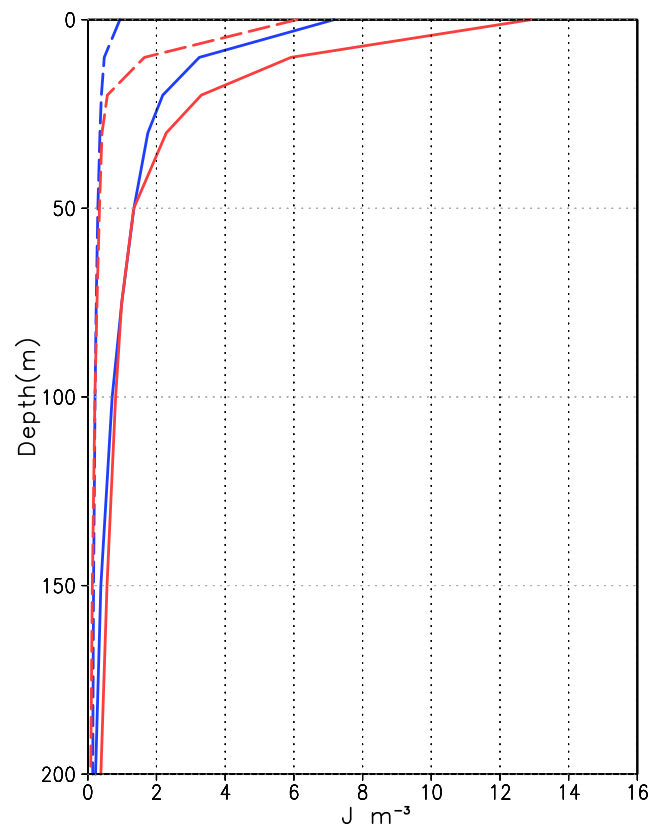


**Fig. 6** Basin-averaged vertical profiles of the EKE (red line) and MKE (blue line) in the Sea of Okhotsk in winter (solid line) and summer (dashed line)

values of the MKE. Both the MKE and EKE, amounting to 8 MKE, attain their minima in summer and a difference between them attains maximal values. According to the vertical profiles of the MKE and EKE, the intensive dynamics is observed in the upper 200 m. Below this depth, both the EKE and MKE values change weakly for both seasons. So, we will consider the EKE in the upper 200 m. Figure 7 shows a spatial distribution of the EKE integrated in the upper 200 m during the year. We find that, in winter the EKE (see Fig. 7a) reaches its maximum along the western boundary of the Sea of Okhotsk, and in the southwestern part of the Kuril Basin near the Kuril Straits. Note that near the western boundary of the Sea of Okhotsk, the spatial structure of EKE is much smoother than the spatial structure of MKE. The smoothness points out a large variability in the positions of mesoscale eddies and other time-varying features captured in EKE. The region with less high values of the EKE covers the continental slope up to 149° E. These features of the spatial structure of EKE could be a consequence of variability of the basin-scale currents captured in EKE in the northwestern Sakhalin shelf. Low values of the EKE are observed over the Kuril Basin, mainly, along the Kuril Straits and near the western coast of the Kamchatka peninsula. Note that high values of



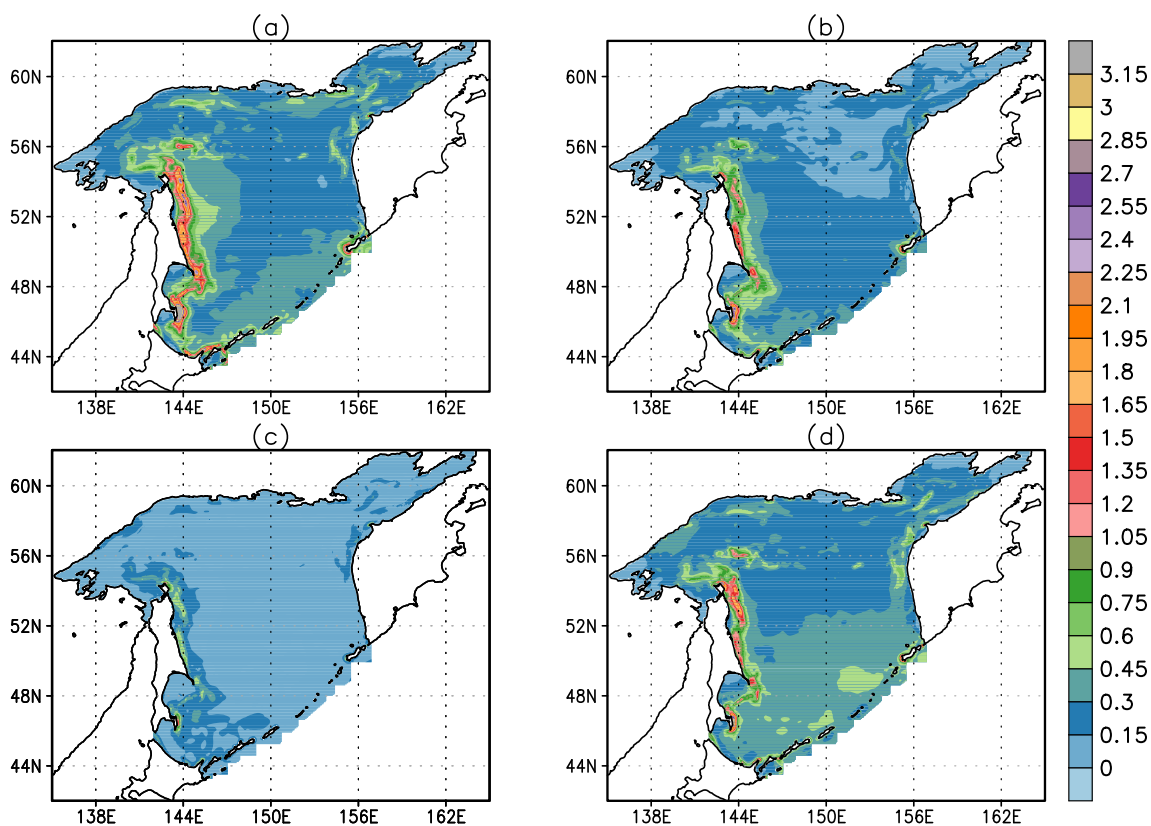


**Fig. 7** Seasonal mean EKE ( $10^3 \text{ J m}^{-2}$ ) integrated in the upper 200 m in **a** winter, **b** spring, **c** summer, and **d** autumn

the EKE are observed over the northwestern shelf of the Sea of Okhotsk. However, these estimations of the EKE could be underestimated due to the used coarse spatial resolution in this region of the Sea of Okhotsk. The intensity of the mesoscale variability decreases noticeably in spring. Maximal values of the EKE are observed, mainly, along the western boundary of the Sea of Okhotsk as well as in the southwestern part of the Kuril Basin. EKE values are lower in the rest of the part of the Sea of Okhotsk. In summer, the EKE shows its minima over the Sea of Okhotsk under its maxima are observed along the western boundary of this sea. In autumn, the intensity of the mesoscale dynamics increases again. The EKE reaches its maxima along the western boundary of the Sea of Okhotsk, in the southern part of the Kuril Basin as well as the western boundary of the Kamchatka peninsula (see Fig. 7d).

Thus, the mesoscale variability of the circulation in the Sea of Okhotsk is more intensive in the upper 200 m, where the EKE values are several times as high the MKE values in winter and up to eight times in summer. The EKE shows the pronounced seasonal variability with its maxima in winter and its minima in summer. According to the spatial distribution of the EKE integrated in the upper 200 m, its extremal values are observed along the western boundary of the Sea of Okhotsk during the year. We suppose that the

observed intensive mesoscale variability could be driven by the hydrodynamic instability of the ESC, which could arise under the weakening of the ESC in response to the decrease of the wind stress from winter to summer. This weakening of the ESC was revealed with the velocity measurements (Mizuta et al. 2003) and the numerical simulation outputs on the coarse resolution (Smizu and Ohshima 2006).

### 5 Eddy energy budget in the Sea of Okhotsk

At examining EKE in the closed basins, the general framework is based on an analysis of the EKE budget as proposed by von Storch et al. (2012). By considering components of the EKE budget, we can assess sinks and sources of the EKE and its dissipation as well as energy conversions between various components of total energy. These estimates are very important at analyzing the mesoscale variability of the circulation as well as heat and freshwater budgets in the Sea of Okhotsk. In this study, impacts of hydrodynamic instability of the basin-scale circulation and wind power input are considered as major sources of the EKE in the Sea of Okhotsk.

To present the EKE budget equation, we consider the known system of equations of the ocean circulation. This

system, formulated in the Boussinesq and hydrostatic approximations, has a form

$$\begin{cases} \frac{d\mathbf{u}_h}{dt} + f\mathbf{k} \times \mathbf{u}_h + \frac{\nabla_h p}{\rho_0} = \frac{\mathbf{F}_h}{\rho_0}, \\ \frac{\partial \hat{p}}{\partial z} = -\rho g, \\ \nabla_h \cdot \mathbf{u}_h + \frac{\partial w}{\partial z} = 0. \end{cases} \quad (13)$$

Here,  $\mathbf{u}_h$  and  $w$  are the vectors of horizontal velocities and vertical velocity, respectively,  $\mathbf{k}$  is the vertical single vector,  $\hat{p}$  is the pressure and  $\mathbf{F}_h$  is the turbulent viscosity, and  $\nabla_h$  is the horizontal nabla operator.

According to these studies (Yang et al. 2013; Zhai and Marshall 2013), the solution of Eq. 13 can be presented as a sum of two components: time-mean and time-varying (turbulent) components. The EKE budget equation with its sources and sinks as well as energy conversion paths has a form

$$\begin{aligned} \nabla \cdot \overline{p'\mathbf{u}'} + \frac{\rho_0}{2} \left( \nabla(\mathbf{u} \cdot \mathbf{u}_h'^2) + \frac{\partial \mathbf{u}_h'^2}{\partial t} \right) &= -\overline{\rho'w'g} + \overline{\mathbf{u}'_h \cdot \mathbf{F}'_h} \\ &- \rho_0 \overline{\mathbf{u}'_h \cdot (\mathbf{u}' \cdot \nabla \mathbf{u}_h)}, \end{aligned} \quad (14)$$

where  $\mathbf{u}$  is the three-dimensional velocity.

In Eq. 14, the first term on the right-hand side (RHS),  $-\overline{\rho'w'g}$ , denotes the rate of energy conversion from eddy available potential energy (EPE) to EKE and measures the strength of baroclinic instability. The second term on the RHS,  $\overline{\mathbf{u}'_h \cdot \mathbf{F}'_h}$  denotes the time-varying component of wind forcing and internal turbulent viscosity induced by sub-grid processes. Last term on the RHS,  $-\rho_0 \overline{\mathbf{u}'_h \cdot (\mathbf{u}' \cdot \nabla \mathbf{u}_h)} = -\rho_0 \left( \overline{u'^2 \frac{\partial \bar{u}}{\partial x}} + \overline{v'^2 \frac{\partial \bar{v}}{\partial y}} + \overline{u'v'} \left( \frac{\partial \bar{v}}{\partial x} + \frac{\partial \bar{u}}{\partial y} \right) \right) - \rho_0 \left( \overline{u'w'} \frac{\partial \bar{u}}{\partial z} - \overline{v'w'} \frac{\partial \bar{v}}{\partial z} \right)$ , denotes the kinetic energy exchange between the mean current and eddies, the latter of which represents the energy transfer due to vertical shear instabilities. This term is fairly small compared to the former.

The first term of Eq. 14 on the left-hand side (LHS),  $\nabla \cdot \overline{p'\mathbf{u}'}$ , denotes the pressure work. The second term on the LHS,  $\frac{\rho_0}{2} \nabla(\mathbf{u} \cdot \mathbf{u}_h'^2)$ , characterizes the change of the EKE induced by advection of the mean current; the third term on the LHS,  $\rho_0 \frac{\partial \mathbf{u}_h'^2}{\partial t}$ , denotes the tendency of the EKE.

### 5.1 Eddy energy from the mean currents in the Sea of Okhotsk

According to the results of Section 4, the EKE reaches its maximum along the western boundary of the Sea of Okhotsk. We suppose that hydrodynamics instability (baroclinic and barotropic) of the alongshore component of the ESC induces the intensive mesoscale variability. To confirm this supposition, two quantities are analyzed in this section. The first quantity ( $BC$ ) quantitatively estimates the rate of energy conversion from mean available potential

energy (MPE) to EPE and characterizes baroclinic instability. The second quantity ( $BT$ ) is linked with the rate of energy conversion from MKE to EKE and characterizes barotropic instability. To estimate the  $BC$ , we use the following relation (Thomson 1984; Eden and Boning 2002; Zhan et al. 2016):

$$BC = -\frac{g^2}{N^2 \rho_0} \left( \overline{u'\rho' \frac{\partial \bar{\rho}}{\partial x}} + \overline{v'\rho' \frac{\partial \bar{\rho}}{\partial y}} \right), \quad (15)$$

where  $\overline{N^2}$  is the basin-averaged square of the buoyancy frequency, and  $\rho$  is the density deflection from  $\rho_0$ . To assess an eddy density flux ( $\mathbf{u}'_h \rho'$ ), we used relation (12). According to relation (15), negative  $BC$  indicates that EPE is converted to MPE, when  $\mathbf{u}'_h \rho'$  is directed in the same direction with the horizontal gradient of the mean density. On the other hand, when the  $BC > 0$ , then  $\mathbf{u}'_h \rho'$  is against the direction of the mean density gradient, that is, MPE is converted to EPE. Figure 8 shows a spatial distribution of the  $BC$ , integrated in the upper 200 m, during the year. We find that  $BC$  reaches its maximum along the western boundary of the Sea of Okhotsk in winter, where the energy conversion between MPE and EPE predominates on the energy conversion from EPE to MPE. In other regions of the Sea of Okhotsk,  $BC$  magnitudes are two times less than those along the western boundary of this sea. In spring,  $BC$  distribution is inhomogeneous. It indicates that both EPE is converted to MPE and MPE is converted to EPE. In summer,  $BC$  reaches its minimum. In autumn, high magnitudes of  $BC$  are observed in the northwestern part of the Sea of Okhotsk.

To analyze a contribution of the horizontal shear of the ESC, associated with barotropic instability,  $BT$  is estimated according to relation (14) as the following:

$$BT = -\rho_0 \left( \overline{u'^2 \frac{\partial \bar{u}}{\partial x}} + \overline{v'^2 \frac{\partial \bar{v}}{\partial y}} + \overline{u'v'} \left( \frac{\partial \bar{v}}{\partial x} + \frac{\partial \bar{u}}{\partial y} \right) \right). \quad (16)$$

Positive  $BT$  characterizes the rate of energy conversion from MKE to EKE and negative  $BT$  characterizes the rate of energy conversion from EKE to MKE. Figure 9 shows a spatial distribution of  $BT$ , integrated in the upper 200 m, during the year. We find that  $BT$  reaches its extremum in winter and autumn. In summer, we observed  $BT$  minima.  $BT$  maxima are observed in the region of the narrow continental shelf and high horizontal shear of the ESC in the northwestern Sakhalin Island. The  $BT$  distributions are inhomogeneous, that is, regions with energy conversion from MKE to EKE alternate with regions, where EKE is converted to MKE. The comparison of the distributions of  $BC$  (see Fig. 8) and  $BT$  (see Fig. 9) points out that along the western boundary of the Sea of Okhotsk, the energy conversion from MPE to EPE predominates over the energy conversion from MKE to EKE in the first half of the year. The distributions of  $BC$  are more homogeneous in contrast to those of  $BT$ . Inhomogeneity of  $BT$  distributions

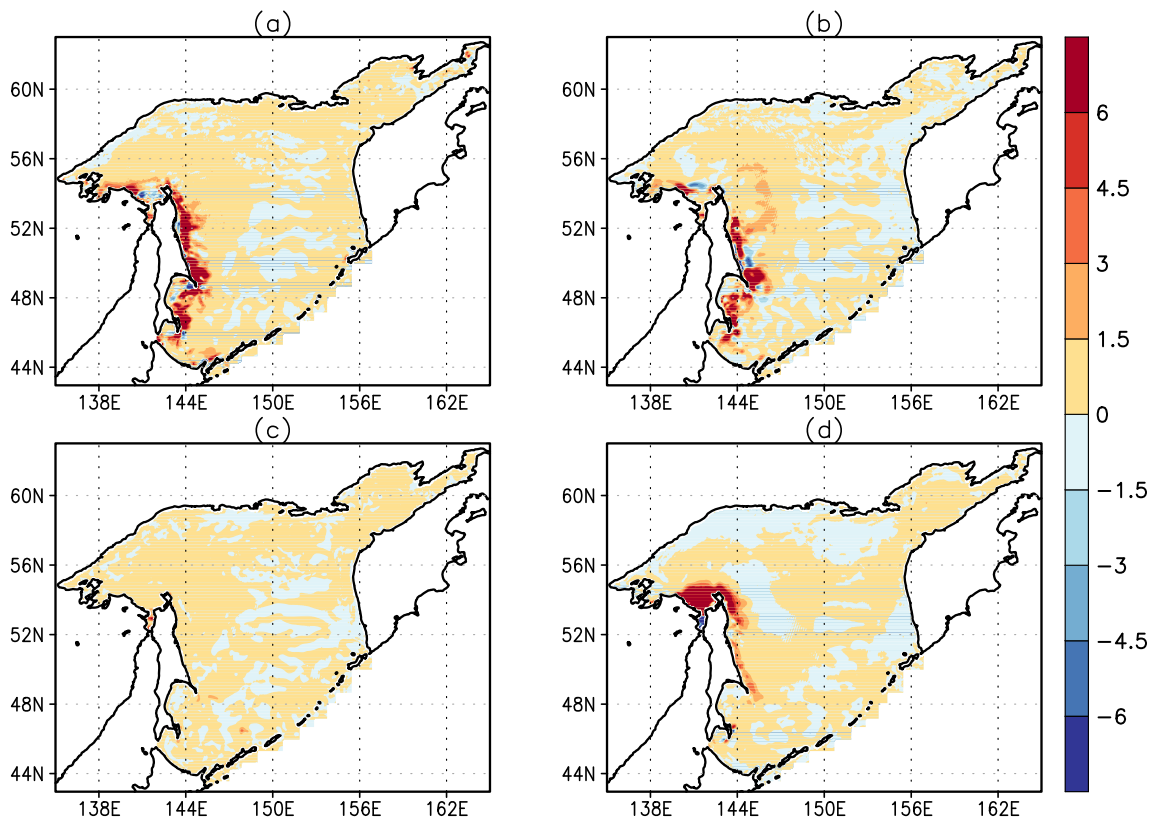


**Fig. 8** Distribution of the MPE-to-EPE term ( $BC$ ) ( $10^{-3} \text{ W m}^{-2}$ ), integrated in the upper 200 m in **a** winter, **b** spring, **c** summer, and **d** autumn

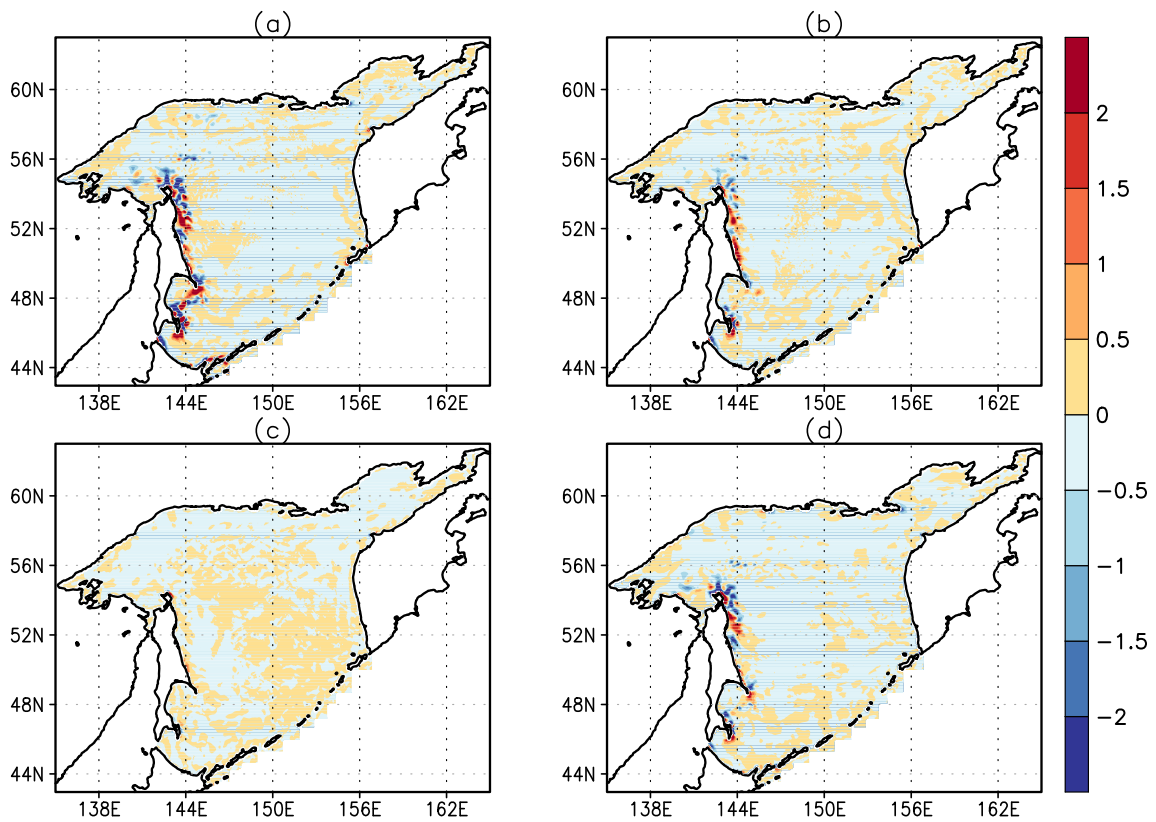


**Fig. 9** Distribution of the MKE-to-EKE term ( $BT$ ) ( $10^{-3} \text{ W m}^{-2}$ ), integrated in the upper 200 m in **a** winter, **b** spring, **c** summer, and **d** autumn

reduces its integral contribution to the EKE in contrast to the integral contribution of the *BC*. Note that along the western boundary of the Sea of Okhotsk, *BT* is one magnitude larger than *BC*. Thus, the presented results indicate that barotropic instability and baroclinic instability can be responsible for the mesoscale variability along the western boundary of the Sea of Okhotsk.

## 5.2 Sources of the EKE in the Sea of Okhotsk

Ohshima et al. (2004) showed that wind stress plays the leading role in the generation of the basin-scale circulation in the Sea of Okhotsk. Positive wind stress curl drives the cyclonic gyre in the central part of the Sea of Okhotsk and the alongshore wind stress component induces the barotropic component of the alongshore branch of the ESC (see Fig. 10a). Seasonal variability of wind stress features the monsoon circulation over the Sea of Okhotsk (see Fig. 10b–d) and drives a strong seasonal variability of the circulation in the Sea of Okhotsk (see Fig. 2), in particular, seasonal variability of the ESC transport (Smizu and Ohshima 2006). It is supposed that wind power input can be one of the major sources of the EKE and mesoscale variability in the Sea of Okhotsk.

According to the EKE budget Eq. 14, one of the sources of the EKE is the wind power input, which is associated with  $(\mathbf{u}'_h \cdot \mathbf{F}'_h)$ . We estimate this source of the EKE as the following. According to the studies (Huang et al. 2006; Zhai et al. 2012; Wunsch 1998),

$$G = \overline{\tau_x \cdot u_s} + \overline{\tau_y \cdot v_s}, \quad (17)$$

where  $\tau_x, \tau_y$  are the wind stress components. Relation (17) can be presented as the following:

$$G = \overline{\tau_x \cdot u_s} + \overline{\tau_y \cdot v_s} = G_1 + G_2, \\ G_1 = \overline{\tau_x \cdot u_s} + \overline{\tau_y \cdot v_s}, \quad G_2 = \overline{\tau'_x \cdot u'_s} + \overline{\tau'_y \cdot v'_s}. \quad (18)$$

Here,  $G_1$  denotes the rate of energy conversion from wind energy to MKE and  $G_2$  denotes the rate of energy conversion from wind energy to EKE, where  $\tau'$  denotes a time-varying component of wind stress. Positive  $G_2$  indicates that the time-varying component of wind stress promotes increasing the EKE on the sea surface and negative  $G_2$  indicates that the time-varying component of wind stress prevents increase of the EKE on the sea surface. Note that in contrast to the approach, presented in these studies (Wunsch 1998; Zhai et al. 2012; Huang et al. 2006), instead of the

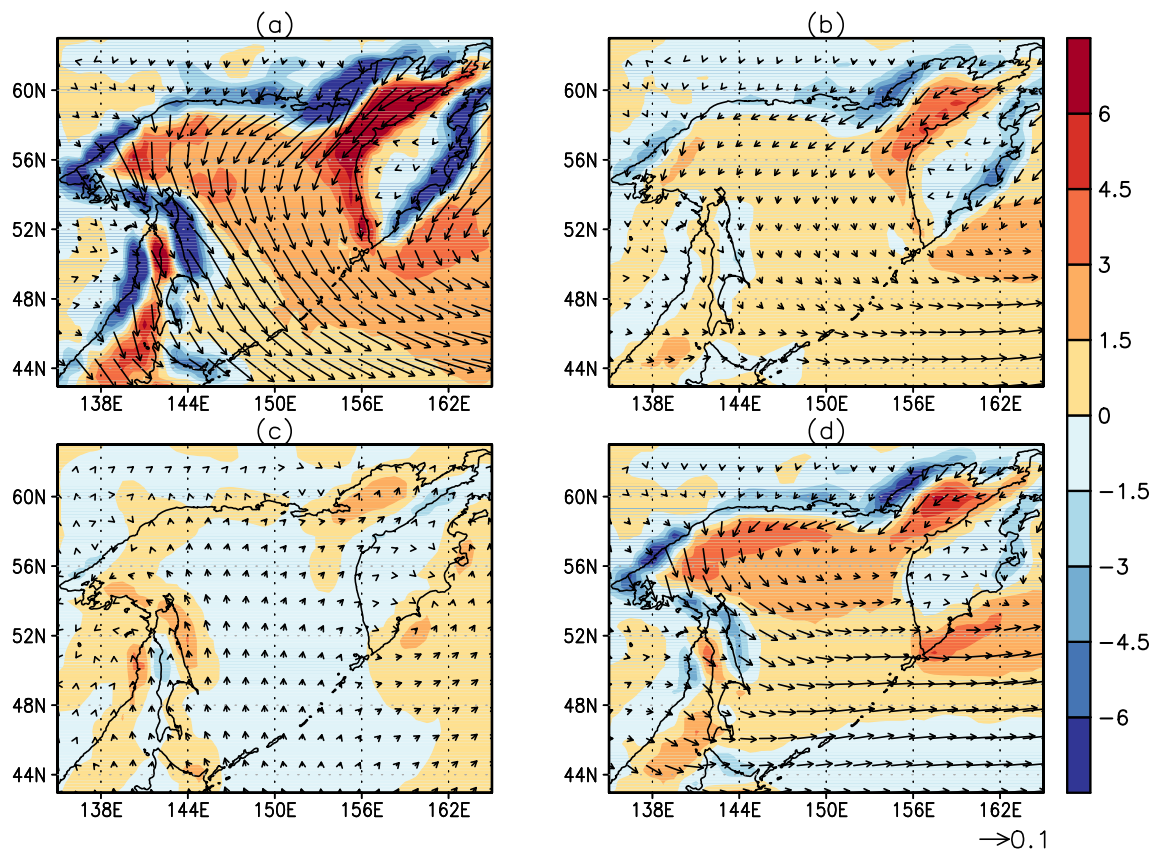


**Fig. 10** Long-term seasonal mean wind stress (vector,  $\text{N m}^{-2}$ ) and wind stress curl ( $10^{-7} \text{ N m}^{-3}$ ) over the Sea of Okhotsk extracted the ERA–Interim dataset accounting for the numerical simulation outputs

geostrophic velocities, we used sea surface velocities.

According to the  $G_2$  distribution, it reaches its maximum in winter (see Fig. 11a). Intensive energy exchange between the time-varying component of wind stress and EKE occurs in the northeastern, southeastern, and western parts of the Sea of Okhotsk. In spring, the  $G_2$  magnitudes decrease over the whole basin (see Fig. 11b). However, high magnitudes of  $G_2$  occur along the western boundary of the Sea of Okhotsk. In summer,  $G_2$  decreases significantly and reaches its minimum over the whole basin, except in a small region, situated along the western boundary of the Sea of Okhotsk (see Fig. 11c). In autumn, the intensity of energy exchange between the time-varying wind stress component and EKE increases in the northern, western, and eastern parts of the Sea of Okhotsk (see Fig. 11d). Thus,  $G_2$  shows its extreme positive values along the western boundary of the Sea of Okhotsk in winter and in summer; that is, the time-varying wind stress promotes increase of the EKE. High values of the  $G_2$  in comparison with  $BC$  values (see Fig. 8) and  $BT$  values (see Fig. 9) indicate a leading role of the time-varying wind stress in the generation of the EKE along the western boundary of the Sea of Okhotsk.

In the preceding subsection, we established that  $BC$  magnitudes exceed those of  $BT$  and baroclinic instability

can be a leading intrinsic source of mesoscale variability over the eastern Sakhalin shelf. According to the study (Zhan et al. 2016), a mechanism of baroclinic instability consists of two stages. On the first stage, the energy conversion from MPE to EPE is realized. On the second stage, EPE is converted to EKE. The intensity of this energy conversion is characterized by a source of the EKE budget Eq. 14, which is given by the relation

$$-\overline{\rho'w'g}, \tag{19}$$

where  $w'$  is the time-varying vertical velocity and  $\rho'$  is the time-varying density component. Positive  $-\overline{\rho'w'g}$  points out denser (later) water masses associated with downward (upward) movements.

Figure 12 shows a spatial distribution of  $-\overline{\rho'w'g}$ , integrated in the upper 200 m, during the year.  $-\overline{\rho'w'g}$  reaches its maximum along the western boundary of the Sea of Okhotsk in winter. The region, where  $-\overline{\rho'w'g}$  reaches its maximum, covers the shelf zone on the western boundary of this sea. In spring, the rate of energy conversion from EPE to EKE decreases in the southwestern part of the Sea of Okhotsk and a distribution of  $-\overline{\rho'w'g}$  is inhomogeneous. In summer, minimal magnitudes of  $-\overline{\rho'w'g}$  are observed over the whole basin. In autumn, the rate of energy conversion

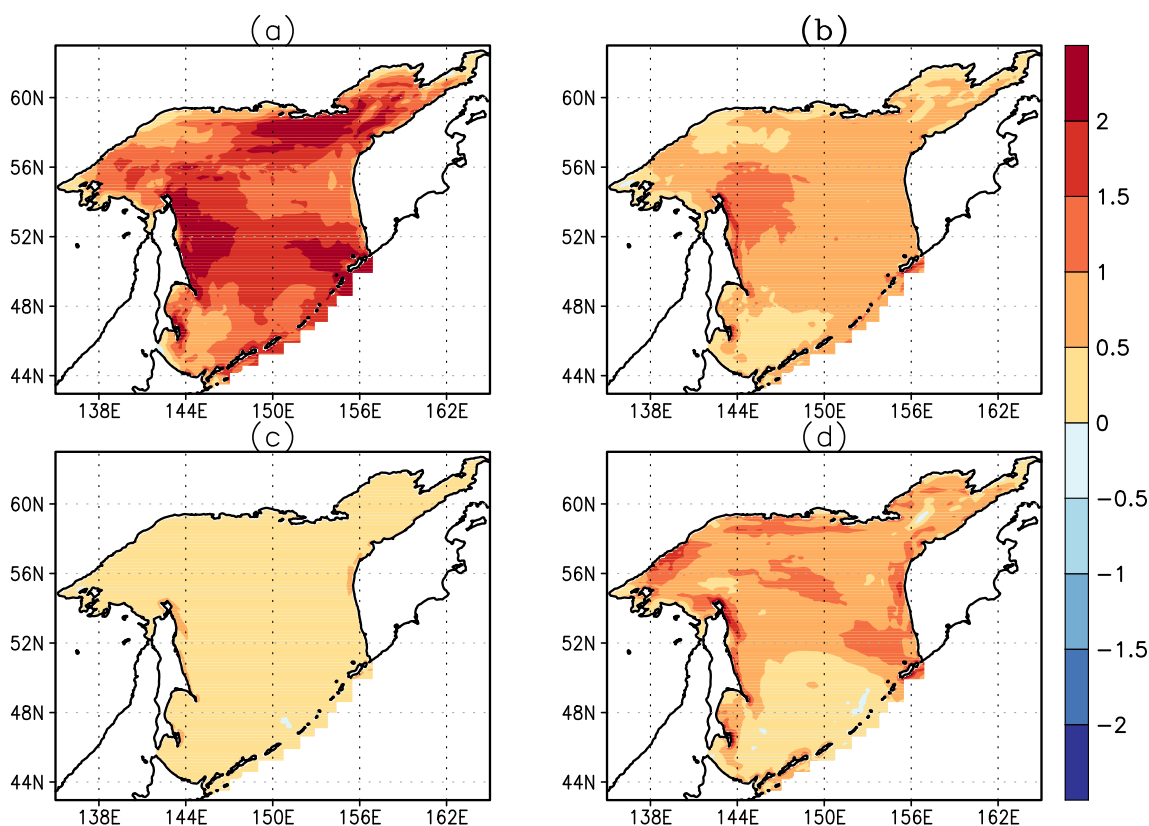


**Fig. 11** Distribution of generation of EKE due to surface power input by the time-varying wind component ( $10^{-2} \text{ W m}^{-2}$ ) in **a** winter, **b** spring, **c** summer, and **d** autumn

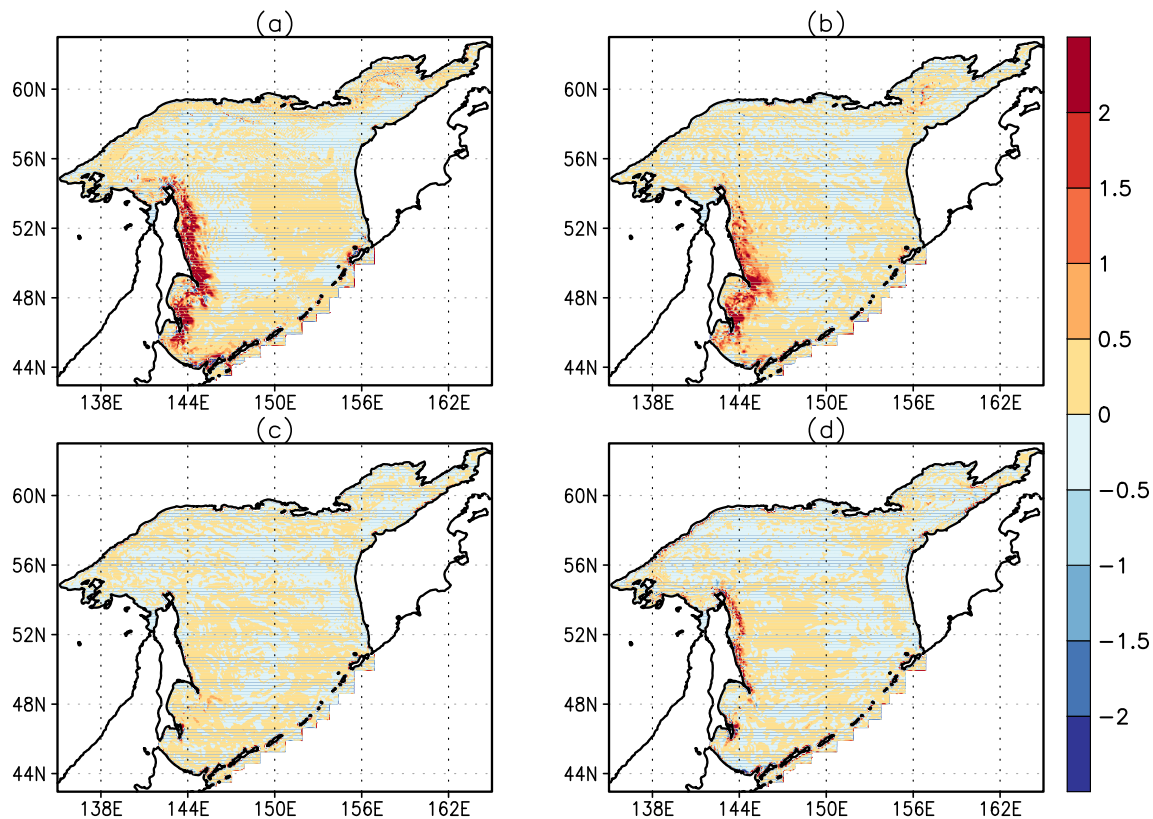


**Fig. 12** Distribution of the EPE-to-EKE term ( $10^{-3} \text{ W m}^{-2}$ ), integrated in the upper 200 m in **a** winter, **b** spring, **c** summer, and **d** autumn

from EPE to EKE increases again along the western boundary of the Sea of Okhotsk and reaches its wintertime magnitudes. However, the distribution of the  $-\overline{\rho'w'g}$  is strongly inhomogeneous in contrast to that in winter. Thus, our analysis of EKE sources shows that the time-varying wind stress component predominates on the other sources of the EKE in the Sea of Okhotsk. However, the domination of the energy conversion from MPE to EPE over the energy conversion from MKE to EKE in winter and autumn, as well as high magnitudes of  $-\overline{\rho'w'g}$ , indicates the importance of baroclinic instability in the generation of mesoscale variability along the western boundary of the Sea of Okhotsk.

### 5.3 Mesoscale eddies on the eastern shelf of Sakhalin Island in spring 2005

In preceding sections, we established that the ESC manifests hydrodynamic instability in winter. In this section, the results of baroclinic instability on the eastern shelf of Sakhalin Island from January to May 2005 are presented. To demonstrate these results, the simulated circulation is considered along the western boundary of the Sea of Okhotsk.

Let us consider velocity field and vertical component of relative vorticity vector (hereinafter, relative vorticity)

which is estimated from the numerical simulation outputs as following the relation  $\xi = \frac{1}{f}(\frac{\partial v}{\partial x} - \frac{\partial u}{\partial y})$ , where  $f = 2\Omega \sin \vartheta$ ,  $\vartheta$  is the latitude, and  $\Omega$  is the Earth rotation rate.

Figure 13 shows velocity and  $\xi$  fields at the depth of 20 m on 9 April 2005. According to the presented velocity field, three eddy structures originate over the eastern Sakhalin shelf. In the moment of their originating, the alongshore component of the ESC follows along the isobaths, ranging from 200 to 240 m, with a mean current velocity amounting to  $0.25\text{--}0.3 \text{ m s}^{-1}$ . In the relative vorticity field, spots with negative  $\xi$ , amounting to about  $-0.3$ , and associating with these eddy structures, are observed. Negative  $\xi$  indicates that these eddy-like structures are anticyclonic eddies.

Figure 14 shows vertical structures of the  $\xi$ ,  $v$ , and  $\rho$  on three zonal transects crossing the eastern shelf of Sakhalin Island (see Fig. 13). The observed eddy structures are characterized by negative  $\xi$ , manifesting in the upper layer from 50 to 200 m, depending on the zonal transect. An analysis of evolution of these anticyclonic eddies shows that they collapse in the middle of May. Thus, a mean lifetime of these eddies amounts to 45 days. To assess a spatial scale ( $L_{\text{eddy}}$ ) of these eddies, the horizontal scale, where meridional velocity changes its sign, is estimated. Under the mean magnitudes of meridional velocity on the periphery of these eddies varying from  $0.26$  to  $0.42 \text{ m s}^{-1}$ , the mean

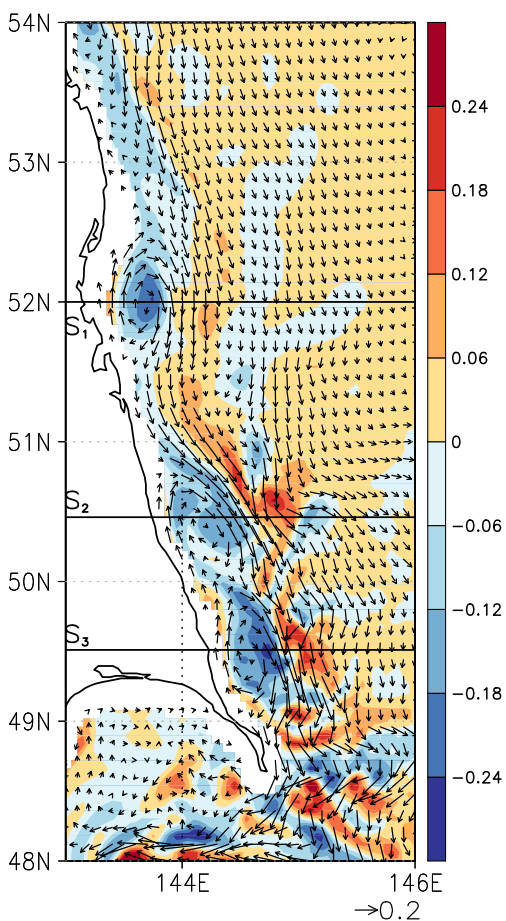


**Fig. 13** Velocity field (vector,  $\text{m s}^{-1}$ ) and vertical component of relative vorticity field (shedding), normalized by the Coriolis frequency, at 20 m depth on the eastern shelf of Sakhalin Island on 9 April 2005.  $S_1$  ( $143^\circ\text{--}144.2^\circ\text{ E}$ ,  $52^\circ\text{ N}$ ),  $S_2$  ( $143.5^\circ\text{--}145^\circ\text{ E}$ ,  $50.46^\circ\text{ N}$ ), and  $S_3$  ( $144^\circ\text{--}145^\circ\text{ E}$ ,  $49.51^\circ\text{ N}$ ) denote three zonal transects

spatial scale of these eddy structures (their diameter) varies from 26 to 34 km. This estimation of the  $L_{eddy}$  coincides with the estimation based on the zonal gradient of the  $\xi$ . Maximal magnitudes of  $v$  are observed from the sea surface to the depths from 60 to 80 m.

According to these studies (Chelton et al. 1998; Stammer 1997), a characteristic spatial scale of mesoscale eddies is close to  $\lambda_1$ . Let us compare  $L_{eddy}$  with  $\lambda_1$ , which is estimated with the relationship (Chelton et al. 1998),

$$\lambda_1 = \frac{c_1}{|f|}, \tag{20}$$

where  $c_1$  is the first eigenvalue satisfying the boundary value problem

$$\begin{aligned} \frac{d^2}{dz^2}\phi_1 + \frac{N^2(z)}{c_1^2}\phi_1 &= 0, \\ \phi_1(0) = \phi_1(-H) &= 0. \end{aligned} \tag{21}$$

Here, a vertical coordinate  $z$  directs from the center of the Earth and  $\phi_1(z)$  is the first eigenfunction of boundary

value problem (21). In this study, the boundary value problem is numerically solved for monthly mean  $N(z)$  profiles, averaged on three zonal transects (see Fig. 13), in April 2005. According to these estimations,  $\lambda_1$  varies from 8 to 12 km. Thus,  $L_{eddy}$  and  $\lambda_1$  are of the same order. In addition, the Rossby number varies from 0.2 to 0.3, that is, these eddy-like structures cover by the quasi-geostrophic dynamics as yet. Therefore, the observed anticyclonic eddies are the mesoscale anticyclonic eddies.

### 6 Discussion

We analyzed the mesoscale variability in the Sea of Okhotsk based on the numerical simulation outputs of the *Control* experiment, which was carried out under the open water approximations (9). Let us consider whether eddy kinetic energy budget changes when the stress on the sea surface takes into account the sea ice cover (hereafter, the *ICE* experiment). In this case, the stress over the sea surface is derived with a bulk formula

$$\tau = A_0\tau_{wind} + (1 - A_0)\tau_{ice}, \tag{22}$$

where  $\tau_{wind}$  is the wind stress over the open water (9),  $A_0$  denotes the ice-free area fraction, and  $\tau_{ice}$  is the ice-water stress estimated with a bulk formula

$$\tau_{ice} = \rho_0 C_{ice} |\mathbf{u}_{ice} - \mathbf{u}_s| (\mathbf{u}_{ice} - \mathbf{u}_s) \tag{23}$$

where  $\mathbf{u}_{ice}$  is the sea ice velocity,  $C_{ice} = 5.5 \times 10^{-3}$ . Initial conditions for model variables correspond to their values on 31 December 2004, derived from the *Control* experiment. Numerical simulations were carried out from 2005 to 2009.

At first, we consider the long-term monthly mean velocity field and the MKE integrated in the upper 200 m derived from the *ICE* experiment (see Fig. 15). According to these distributions, the cyclonic circulation predominates in the Sea of Okhotsk. Along the western boundary of this sea, we observe the ESC that consists of alongshore and offshore components. The offshore component is a part of the cyclonic gyre spanning the Central Basin of the Sea of Okhotsk. The alongshore component follows over the eastern Sakhalin shelf and reach the northeastern coast of Hokkaido Island. The features of the basin-scale circulation and its intensity derived from the *ICE* experiment are very similar these derived from the *Control* experiment. In addition, the seasonal variability of the basin-scale circulation from the *ICE* experiment is consistent with the basin-scale circulation from the *Control* experiment. However, the alongshore component of the ESC from the *Control* experiment is more intensive than that derived

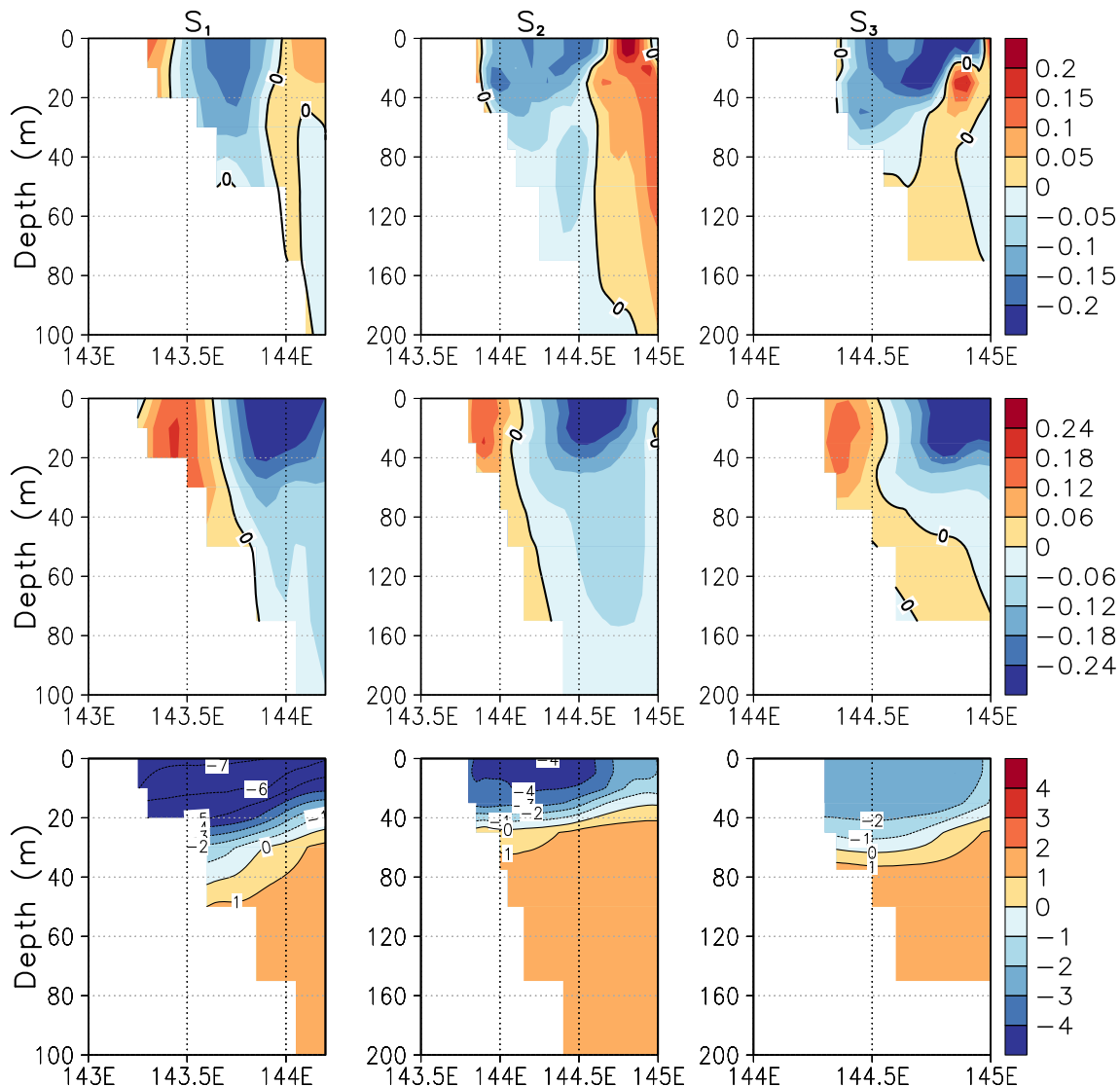


**Fig. 14** Vertical structure at three zonal transects (see Fig. 12): (upper row) vertical component of relative vorticity, normalized by the Coriolis frequency, (middle row) meridional velocity ( $\text{m s}^{-1}$ ), and (down row) density deviation from the reference value of  $1025 \text{ kg m}^{-3}$  on 9 April 2005

from the *ICE* experiment. Thus, the basin-scale circulation structure and its intensity are changed insignificantly when the stress on the sea surface accounting for the sea ice cover.

Let us consider spatial features of the EKE distribution derived from the *ICE* experiment. Figure 16 shows a difference between the EKE derived from the *Control* experiment and that derived from the *ICE* experiment. We find that the maximal difference (about 10%) is observed, mainly, over the eastern Sakhalin shelf and over the continental slope; the difference does not exceed 3% in winter and spring. In the second half of the year, this difference is minimal (about 1%). Thus, accounting for the sea ice cover at the estimation of the stress leads to the insignificant decreasing of the intensity of the mesoscale variability along the western boundary of the Sea of Okhotsk in the first half of the year. Let us consider the

EKE and MKE integrated over the Sea of Okhotsk for both experiments (see Fig. 17). We find that, for both experiments, the EKE is several times as high as the MKE. In addition, the pronounced seasonal variability of the EKE and MKE is observed for both experiments. Maximal values of the EKE and MKE are observed from autumn to winter and their minimal values are observed in summer. Our comparison shows that significant differences between both the MKE and the EKE are observed from January to April due to the sea ice cover. In the *Control* experiment, the circulation energy is overestimated. However, this overestimation is insignificant (no more 10%).

In the end of this section, let us consider the contribution of each component of the EKE budget in its balance. We estimated rates of energy conversion and two EKE sources, integrated in the upper 200 m on the eastern Sakhalin



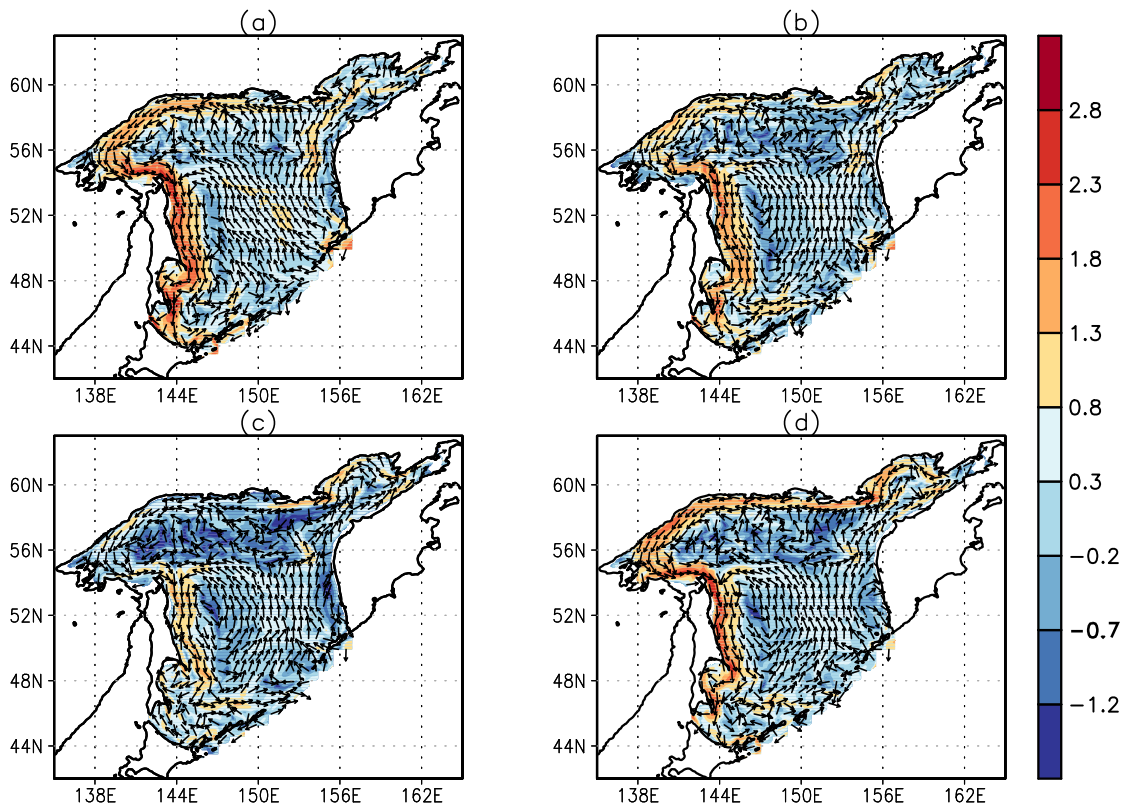


**Fig. 15** Seasonal mean velocity field (vector,direction) and MKE (log<sub>10</sub> cm<sup>2</sup> s<sup>-2</sup>) at 30 m depth obtained from the *ICE* experiment outputs in a winter, b spring, c summer, and d autumn

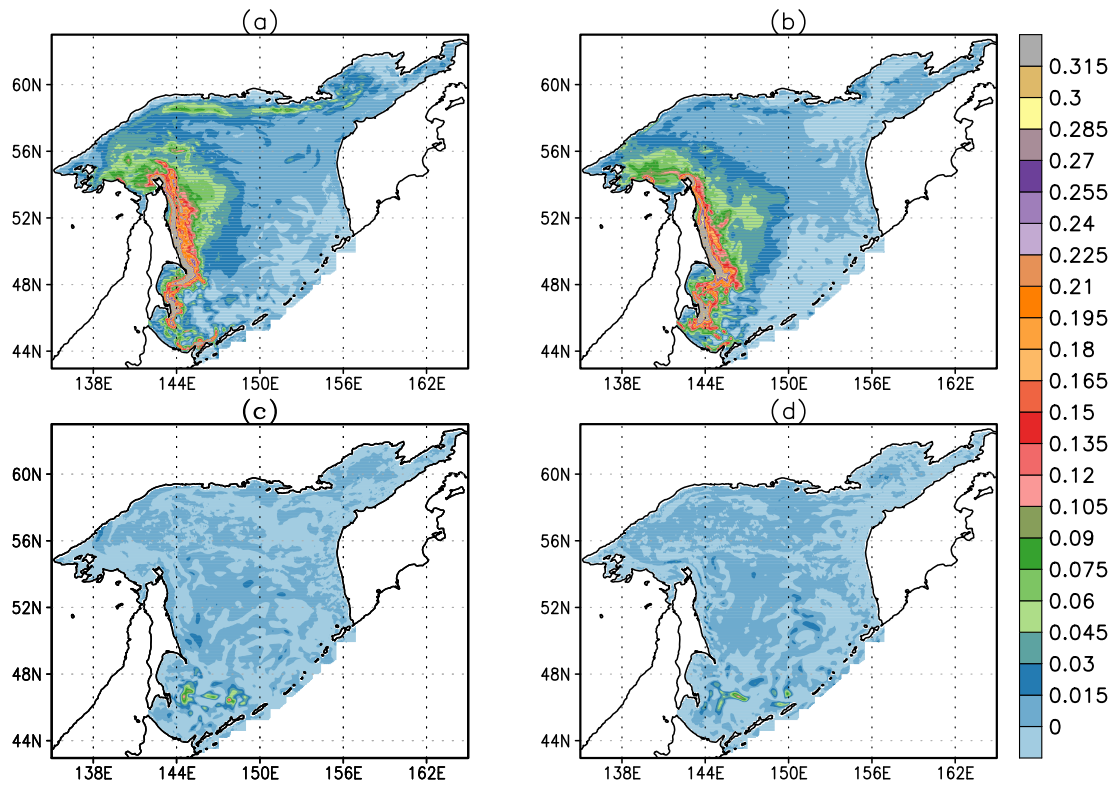
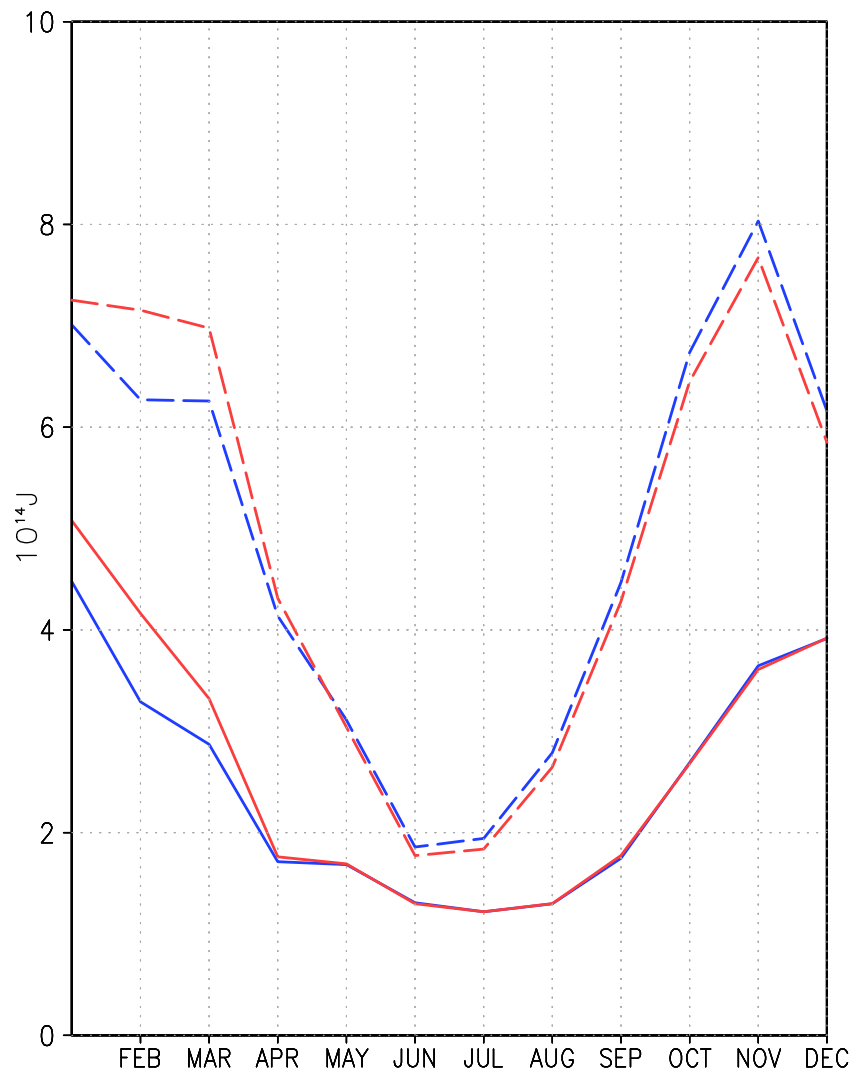


**Fig. 16** Seasonal mean difference (10<sup>3</sup> J m<sup>-2</sup>) between the EKE obtained from the *Control* experiment and that from the *ICE* experiment integrated in the upper 200 m in a winter, b spring, c summer, and d autumn

**Fig. 17** Basin-integrated long-term monthly mean MKE (solid line) and EKE (dashed line) obtained from the *Control* experiment (red line) and the *ICE* experiment (blue line)



shelf during the year for (*Control* and *ICE*) experiments (see Table 1). According to these estimations, a major contribution in the EKE generation brings in the time-varying wind power input (about 4 GW), and the rate of energy conversion from MPE to EPE amounts to about 1 GW, as well as the rate of energy conversion from EPE to EKE amounts to 0.2 GW. Negative *BT* points out a

domination of the EKE to MKE conversion and the rate of this conversion amounts to less  $-0.005$  GW. Low rate of this energy conversion results from high inhomogeneous of the *BT* distribution (see Fig. 9). Minimal values for all variables were observed in summer. Note that a ratio between contributions of the different components of the EKE budget persists in the *ICE* experiment.

**Table 1** Seasonal mean rate of energy conversion between EPE and EKE ( $-\overline{\rho'w'g}$ ), rate of energy conversion between wind energy and EKE ( $\overline{\tau' \cdot \mathbf{u}'_s}$ ), rate of energy conversion between MPE and EPE (*BC*), and rate of energy conversion between MKE and EKE (*BT*) integrated from the sea surface to the depth of 200 m on the eastern Sakhalin shelf

Season	$BT = -\rho_0 \overline{\mathbf{u}'_h \cdot (\mathbf{u}' \cdot \nabla \mathbf{u}'_h)}$	$BC = -\frac{g^2}{N^2 \rho_0} \overline{\mathbf{u}'_h \rho' \cdot \nabla_h \bar{\rho}}$	$\overline{\tau' \cdot \mathbf{u}'_s}$	$-\overline{\rho'w'g}$
Winter	$-4.9(\mathbf{4.5}) \cdot 10^{-3}$	0.8( <b>0.7</b> )	4.0( <b>4.0</b> )	0.18( <b>0.19</b> )
Spring	$-5.7(\mathbf{1.4}) \cdot 10^{-3}$	0.4( <b>0.31</b> )	2.1( <b>1.84</b> )	0.11( <b>0.084</b> )
Summer	$13.0(-\mathbf{1.4}) \cdot 10^{-4}$	0.05( <b>0.07</b> )	0.64( <b>0.9</b> )	$-1.6(\mathbf{4.6}) \cdot 10^{-3}$
Autumn	$-14.0(-\mathbf{1.5}) \cdot 10^{-3}$	0.4( <b>0.4</b> )	1.7( <b>2.83</b> )	$-3.4(\mathbf{27.0}) \cdot 10^{-3}$

Bold symbols denote values derived from the *ICE* experiment. Unit is in  $10^9$  W

## 7 Summary and conclusions

Based on numerical simulation outputs of the INMOM with an eddy-permitting resolution, analysis of the eddy kinetic energy budget revealed features of the mesoscale variability in the Sea of Okhotsk from 2005 to 2009. Validation of the simulated circulation showed that a subsurface velocity field reproduces basic elements of the basin-scale circulation in the Sea of Okhotsk: the West-Kamchatka Current, the cyclonic gyre in the central part of this sea, and the East-Sakhalin Current following along the western boundary of this sea.

Comprehensive analysis of the spatial and temporal variability of the simulated circulation on the western boundary of the Sea of Okhotsk confirmed that East-Sakhalin Current consists of alongshore and offshore components. The alongshore component, originating on the northwestern shelf of the Sea of Okhotsk, follows over the eastern Sakhalin shelf and reaches the northeastern coast of Hokkaido Island. The offshore component of the East-Sakhalin Current follows over the continental slope and turns to the east at 47°–48° N. Numerical simulations revealed a pronounced seasonal variability of the transport of the East-Sakhalin Current, which reaches its maximum (about 6 Sv) in winter and decreases up to 1–1.5 Sv in summer. Analysis of the vertical structure of the simulated potential density revealed that isopycnals rise from the east to the west and sharply drop near the western boundary of the Sea of Okhotsk. It is consistent with the vertical structure of the density derived from observations and confirms that the simulated offshore component is an analog of the western boundary current. Analysis of the eddy kinetic energy pointed out that the intensive mesoscale variability is observed in the upper 200 m. The EKE values exceed the MKE values in the course of year.

The EKE showed a pronounced seasonal variability with maximal values in winter and minimal values in summer. Spatial distribution of the EKE integrated in the upper 200 m showed that in the course of year its maximal values were observed along the western boundary of the Sea of Okhotsk and associated with the alongshore component of the East-Sakhalin Current. Spatial distribution of the rate of energy conversion from MKE to EKE ( $BT$ ) characterizing mechanism of barotropic instability showed that  $BT$  reaches its extremal values in winter and autumn and its minimal magnitudes were observed in summer along the western boundary of the Sea of Okhotsk. Spatial distributions of  $BT$  were strongly inhomogeneous. It points out that the eastern Sakhalin shelf is a zone of intensive conversion between the MKE to EKE and EKE to MKE. In summer, the rate of energy conversion from MKE to EKE decreases notably due to the weakening of the East-Sakhalin Current and its horizontal shear. To analyze the baroclinic instability,

we considered two characteristics:  $BC$  and  $-\overline{\rho'w'g}$ . It was established that a high rate of conversion from MPE to EPE was observed on the eastern Sakhalin shelf in winter. Domination of positive values of the  $BC$  indicates that the conversion from MPE to EPE predominates on the contrary conversion from EPE to MPE. The rate of energy conversion from EPE to EKE reaches its maximum in winter. The maximal values of  $-\overline{\rho'w'g}$  are associated with the East-Sakhalin current and cover the whole eastern Sakhalin shelf in winter. In autumn, the region with maximal values of  $-\overline{\rho'w'g}$  is narrowed. Because the basin-scale circulation in the Sea of Okhotsk and its seasonal variability are driven by wind stress, we considered a time-varying component of the wind power as one of the main sources of the EKE. According to distributions of the time-varying wind power component, its maximal values were observed on the eastern Sakhalin shelf and in the northeastern part of the Sea of Okhotsk. In summer, the time-varying wind power component reaches its minimal values and increases in autumn.

Comparison of the rates of energy conversion and two EKE sources, integrated in the upper 200 m on the eastern Sakhalin shelf, showed that major sources of the EKE are the time-varying wind power input and baroclinic instability characterized by the pronounced seasonal variability. A leading role of baroclinic instability relative to barotropic instability in the generation of the EKE along the western boundary of the Sea of Okhotsk is consistent with the importance of this mechanism in the generation of the mesoscale variability both the World Ocean and marginal seas (Stammer 1997). The direct action of wind, particularly, its time-varying component, also plays a leading role in the generation of the EKE.

To reveal a manifestation of the baroclinic instability mechanism on the eastern Sakhalin shelf, we analyzed velocity and relative vorticity fields in spring 2005. We established that from March to April, the anticyclonic mesoscale eddies were generated on the eastern Sakhalin shelf. Spatial scales of these eddies, varying from 25 to 34 km and their lifetime equals about 45 days. These observed anticyclonic mesoscale eddies generate an eddy buoyancy flux that relates closely with the eddy heat flux (Wolfe et al. 2008). Intensive vertical eddy buoyancy flux results in more intensive vertical mixing on the eastern Sakhalin shelf. Thus, the revealed features of mesoscale dynamics point out more complicated dynamics on the eastern Sakhalin shelf, which need to take into account under analyzing advection of the dense shelf water by the East-Sakhalin Current and ecosystem of the eastern Sakhalin shelf and its evolution.

**Acknowledgments** The numerical simulation outputs were obtained using the equipment of Shared Resource Center “Far Eastern Computing Resource” IACP FEB RAS (<https://www.cc.dvo.ru>).

**Funding information** This work was supported by the RFBF (projects N 17-05-00035 and N 18-05-01107), and a part of the work was supported by the POI FEBRAS Program “Mathematical simulation and analysis of dynamical processes in the ocean” No. 117030110034-7.

## References

- Becker J, Sandwell D, Smith W, Braud J, Binder B, Depner J, Fabre D, Factor J, Ingalls S, Kim SH, Ladner R, Marks K, Nelson S, Pharaoh A, Trimmer R, Rosenberg J, Wallace G, Weatherall P (2009) Global bathymetry and elevation data at 30 arc seconds resolution: SRTM30 PLUS. *Mar Geod* 32:355–371. <https://doi.org/10.1080/01490410903297766>
- Brydon D, Sun S, Bleck R (1999) A new approximation of the equation of state for seawater, suitable for numerical ocean models. *J Geophys Res* 104:1537–1540. <https://doi.org/10.1029/1998JC900059>
- Chelton D, deSzoeke R, Schlax M (1998) Geographical Variability of the First Baroclinic Rossby radius of deformation. *J Phys Oceanogr* 28:433–460. [https://doi.org/10.1175/1520-0485\(1998\)028<0433:GVOTFB>2.0.CO;2](https://doi.org/10.1175/1520-0485(1998)028<0433:GVOTFB>2.0.CO;2)
- Chelton D, Schlax M, Samelson R (2011) Global observations of nonlinear mesoscale eddies. *Prog Oceanogr* 91:167–216. <https://doi.org/10.1016/j.pocean.2011.01.002>
- Dee DP, Uppala SM, Simmons AJ, Berrisford P, Poli P, Kobayashi S, Andrae U, Balmaseda MA, Balsamo G, Bauer P, Bechtold P, Beljaars ACM, van de Berg L, Bidlot J, Bormann N, Delsol C, Dragani R, Fuentes M, Geer AJ, Haimberger L, Healy SB, Hersbach H, Holm EV, Isaksen L, Kallberg P, Kohler M, Matricardi M, McNally AP, Monge-Sanz BM, Morcrette JJ, Park BK, Peubey C, de Rosnay P, Tavolato C, Thepaut JN, Vitart F (2011) The ERA-Interim reanalysis: configuration and performance of the data assimilation system. *Q J Roy Meteor Soc* 137:553–597. <https://doi.org/10.1002/qj.828>
- Diansky N, Stepanov D, Gusev V, Novotryasov V (2016) Role of wind and thermal forcing in the formation of the water circulation variability in the Japan/East Sea Central Basin in 1958–2006. *Izv Atmos Ocean Phys* 52:207–216. <https://doi.org/10.1134/S0001433816010023>
- Eden C, Boning C (2002) Sources of Eddy Kinetic Energy in the Labrador Sea. *J Phys Oceanogr* 32:3346–3363. [https://doi.org/10.1175/1520-0485\(2002\)032<3346:SOEKEI>2.0.CO;2](https://doi.org/10.1175/1520-0485(2002)032<3346:SOEKEI>2.0.CO;2)
- Ferrari R, Wunsch C (2010) The distribution of eddy kinetic and potential energies in the global ocean. *Tellus A* 62:92–108. <https://doi.org/10.3402/tellusa.v62i2.15680>
- Fukamachi Y, Mizuta G, Ohshima K, Talley L, Riser S, Wakatsuchi M (2004) Transport and modification processes of dense shelf water revealed by long-term moorings off Sakhalin in the Sea of Okhotsk. *J Geophys Res* 109:2156–2202. <https://doi.org/10.1029/2003JC001906>
- Gladyshov S, Talley L, Kantalov G, Khen G, Wakatsuchi M (2003) Distribution, formation, and seasonal variability of Okhotsk Sea mode water. *J Geophys Res* 108:2156–2202. <https://doi.org/10.1029/2001JC000877>
- Gusev AV, Diansky NA (2014) Numerical simulation of the World ocean circulation and its climatic variability for 1948–2007 using the INMOM. *Izv Atmos Ocean Phys* 50:1–12. <https://doi.org/10.1134/S0001433813060078>
- Huang R, Wang W, Liu L (2006) Decadal variability of wind-energy input to the World Ocean. *Deep-Sea Res II* 53:31–41. <https://doi.org/10.1016/j.dsr2.2005.11.001>
- Koshlyakov M, Monin A (1978) Synoptic eddies in the ocean. *Annu Rev Earth Planet Sci* 6:495–523
- Lapeyre G (2009) What vertical mode does the altimeter reflect? On the decomposition in baroclinic modes and on a surface-trapped mode. *J Phys Oceanogr* 39:2857–2874. <https://doi.org/10.1175/2009jpo3968.1>
- Large W, Yeager S (2009) The global climatology of an inter-annually varying air–sea flux data set. *J Clim* 33:341–364. <https://doi.org/10.1007/s00382-008-0441-3>
- Locarnini R, Mishonov A, Antonov JI, Boyer T, Garcia H, Baranova O, Zweng M, Paver C, Reagan J, Johnson D, Hamilton M, Seidov D (2013) World Ocean Atlas 2013, Volume 1: Temperature. Tech. rep. <https://www.nodc.noaa.gov/OC5/woa13/pubwoa13.html>
- Luchin V (1998) Hydrometeorological condition: steady current (in Russian), vol 9. The Okhotsk Sea, Gidrometeoizdat, pp 233–256
- Marchuk GI, Rusakov AS, Zalesny VB, Diansky NA (2005) Splitting numerical technique with application to the high resolution simulation of the Indian ocean circulation. *Pure Appl Geophys* 162:1407–1429. <https://doi.org/10.1007/s00024-005-2677-8>
- Matsuda J, Mitsudera H, Nakamura M, Sasajima Y, Hasumi H, Wakatsuchi M (2015) Overturning circulation that ventilates the intermediate layer of the Sea of Okhotsk and the North Pacific: the role of salinity advection. *J Geophys Res* 120:1462–1489. <https://doi.org/10.1002/2014JC009995>
- Mizuta G, Fukamachi Y, Ohshima K, Wakatsuchi M (2003) Structure and seasonal variability of the East Sakhalin Current. *J Phys Oceanogr* 33:2430–2445. [https://doi.org/10.1175/1520-0485\(2003\)033<2430:SASVOT>2.0.CO;2](https://doi.org/10.1175/1520-0485(2003)033<2430:SASVOT>2.0.CO;2)
- Nakamura T, Matthews J, Awaji T, Mitsudera H (2012) Submesoscale eddies near the Kuril Straits: asymmetric generation of clockwise and counterclockwise eddies by barotropic tidal flow. *J Geophys Res* 117:C12014. <https://doi.org/10.1029/2011JC007754>
- Ohshima K, Wakatsuchi M (1990) A numerical study of barotropic instability associated with the Soya Warm Current in the Sea of Okhotsk. *J Phys Oceanogr* 20:570–584
- Ohshima K, Wakatsuchi M, Fukamachi Y (2002) Near-surface circulation and tidal currents of the Okhotsk Sea observed with satellite-tracked drifters. *J Geophys Res* 107:3195
- Ohshima K, Smizu D, Itoh M, Mizuta G, Fukamachi Y, Riser S, Wakatsuchi M (2004) Sverdrup balance and the cyclonic gyre in the Sea of Okhotsk. *J Phys Oceanogr* 34:513–525
- Ohshima K, Fukamachi Y, Mutoh T, Wakatsuchi M (2005) A generation mechanism for mesoscale eddies in the Kuril basin of the Okhotsk Sea: baroclinic instability caused by enhanced tidal mixing. *J Oceanogr* 61:247–260
- Pacanowski R, Philander S (1981) Parameterization of vertical mixing in numerical models of tropical oceans. *J Phys Oceanogr* 11:1443–1451. [https://doi.org/10.1175/1520-0485\(1981\)011<1443:POVMIN>2.0.CO;2](https://doi.org/10.1175/1520-0485(1981)011<1443:POVMIN>2.0.CO;2)
- Pedlosky J (1987) *Geophysical fluid dynamics*. Springer, New York. <https://doi.org/10.1007/978-1-4612-4650-3>
- Shcherbina A, Talley L, Rudnick D (2004) Dense water formation on the northwestern shelf of the Okhotsk Sea: 1. Direct observations of brine rejection. *J Geophys Res* 109:C09S08. <https://doi.org/10.1029/2003JC002196>
- Smizu D, Ohshima K (2006) A model simulation on the circulation in the Sea of Okhotsk and the East Sakhalin Current. *J Geophys Res* 111:C05016. <https://doi.org/10.1029/2005JC002980>
- Stammer D (1997) Global characteristics of ocean variability estimated from regional TOPEX/POSEIDON Altimeter measurements. *J Phys Oceanogr* 27:1743–1769. [https://doi.org/10.1175/1520-0485\(1997\)027<1743:GCOOVE>2.0.CO;2](https://doi.org/10.1175/1520-0485(1997)027<1743:GCOOVE>2.0.CO;2)
- Stepanov D (2017) Estimating the baroclinic Rossby radius of deformation in the Sea of Okhotsk. *Russ Meteorol Hydrol* 42:601–606. <https://doi.org/10.3103/S1068373917090072>

- Stepanov D, Diansky N, Novotryasov V (2014) Numerical simulation of water circulation in the central part of the Sea of Japan and study of its long-term variability in 1958–2006. *Izv Atm Ocean Phys* 50:73–84. <https://doi.org/10.1134/S0001433813050149>
- Talley L (1991) An Okhotsk Sea water anomaly: implications for ventilation in the North Pacific. *Deep-Sea Res I* 38:S171–S190. [https://doi.org/10.1016/S0198-0149\(12\)80009-4](https://doi.org/10.1016/S0198-0149(12)80009-4)
- Thomson R (1984) A cyclonic eddy over the continental margin of Vancouver Island evidence for baroclinic instability. *J Phys Oceanogr* 14:1326–1348
- Uchimoto K, Mitsudera H, Ebuchi N, Miyazawa Y (2007) Anticyclonic eddy caused by the Soya Warm Current in an Okhotsk OGCM. *J Oceanogr* 63:379–391
- von Storch JS, Eden C, Fast I, Haak H, Hernandez-Deckers D, Maier-Reimer E, Marotzke J, Stammer D (2012) An estimate of the Lorenz energy cycle for the World Ocean based on the 1/10 STORM/NCEP simulation. *J Phys Oceanogr* 42:2185–2205. <https://doi.org/10.1175/JPO-D-12-079.1>
- Wolfe C, Cessi P, McClean J, Maltrud M (2008) Vertical heat transport in eddying ocean models. *Geophys Res Lett* 35:L23605. <https://doi.org/10.1029/2008GL036138>
- Wunsch C (1998) The work done by the wind on the oceanic general circulation. *J Phys Oceanogr* 28:2332–2340
- Yakovlev N (2003) Coupled model of ocean general circulation and sea ice evolution in the Arctic Ocean. *Izv Atmos Ocean Phys* 39:355–368
- Yang H, Wu L, Liu H, Yu Y (2013) Eddy energy sources and sinks in the South China Sea. *J Geophys Res* 118:4716–4726. <https://doi.org/10.1002/jgrc.20343>
- Zalesny VB, Agoshkov VI, Aps R, Shutyaev V, Zayachkovskiy A, Goerlandt F, Kujala P (2017) Numerical modeling of marine circulation, pollution assessment and optimal ship routes. *J Mar Sci Eng* 5:27. <https://doi.org/10.3390/jmse5030027>
- Zhai X, Marshall D (2013) Vertical eddy energy fluxes in the North Atlantic Subtropical and Subpolar Gyres. *J Phys Oceanogr* 43:95–103. <https://doi.org/10.1175/JPO-D-12-021.1>
- Zhai X, Johnson H, Marshall D, Wunsch C (2012) On the wind power input to the Ocean General Circulation. *J Phys Oceanogr* 42:1357–1365. <https://doi.org/10.1175/JPO-D-12-09.1>
- Zhan P, Subramanian A, Yao F, Kartadikara A, Guo D, Hotei I (2016) The eddy kinetic energy budget in the Red Sea. *J Geophys Res* 121:4732–4747. <https://doi.org/10.1002/2015JC011589>
- Zweng M, Reagan J, Antonov J, Locarnini R, Mishonov A, Boyer T, Garcia H, Baranova O, Johnson D, Seidov D, Biddle M (2013) World Ocean Atlas 2013, Volume 2: Salinity. Tech. rep. <https://www.nodc.noaa.gov/OC5/woa13/pubwoa13.html>